Monthly Notices
of the
ROYAL ASTRONOMICAL SOCIETY

MNRAS **462,** S376–S393 (2016) doi:10.1093/mnras/stw2859
Advance Access publication 2016 November 8

Mt. Wendelstein imaging of the post-perihelion dust coma of 67P/Churyumov–Gerasimenko in 2015/2016

Hermann Boehnhardt,[1⋆] Arno Riffeser,[2] Matthias Kluge,[2] Christoph Ries,[2] Michael Schmidt[2] and Ulrich Hopp[2]

[1] *Max-Planck Institute for Solar System Research, Justus-von-Liebig-Weg 3, D-37077 Göttingen, Germany*
[2] *University Observatory, Ludwig-Maximilian-University Munich, Scheiner Str. 1, D-81679 München, Germany*

Accepted 2016 November 3. Received 2016 November 3; in original form 2016 June 27

ABSTRACT

Comet 67P/Churyumov-Gerasimenko (67P) was imaged with the 2 m telescope at Mt. Wendelstein Observatory in the Alps. Coma and tail monitoring was performed during 51 nights between 2015 August 22 and 2016 May 9. The images through *r* and *i* Sloan Digital Sky Survey (SDSS) filters show the dust distribution around the comet, while images in the SDSS *g* filter also indicate the presence of coma gas in early 2015 September. The dust colour of 67P implies intrinsic reddening of 9 per cent/100 nm. After maximum, shortly after perihelion passage, the dust activity decreased with a heliocentric exponent of 4.1–4.2 from late 2015 September until 2016 May. The opposition surge during early 2016 can be explained by a linear light scattering phase function ($\beta \sim 0.04$) or an asteroid-like HG-type phase function ($G \sim 0.15$). The radial brightness profile indicates a 'quasi-steady-state' dust coma from late September to the end of 2015. Dust fragmentation during about a month after perihelion may be responsible for radial coma profiles with slopes below unity, while dust accumulation due to very slow dust expansion velocity may result in steeper than unity profiles during 2016. Three fan-shape dust structures are characterized in the coma of 67P. A short dust ejection event on 2015 August 22–23 has produced a dust arc-let and jet feature in the coma. In 2015 September, the appearance of cometary dust tail is dominated by the young dust produced around perihelion. The older dust dominates the tail appearance as of 2015 mid-November.

Key words: comets: individual: 67P/Churyumov-Gerasimenko.

1 INTRODUCTION

In 2015, comet 67P/Churyumov–Gerasimenko (67P), a Jupiter family comet (JFC) and the main science target of ESA's Rosetta mission had its eighth return to perihelion since its discovery on 1969 September 9 at the Alma Ata Observatory. Since 2003, when ESA selected 67P as the main target for Rosetta, the comet received much more attention by regular telescopic observations from Earth and in space in preparation and support of the mission (Schulz, Stüwe & Boehnhardt 2004; Weiler et al. 2004; Lara et al. 2005; Kelley et al. 2006, 2009; Lamy et al. 2006, 2008; Schleicher 2006; Lara, Lin & Rodrigo 2011; Ishiguro 2008; Kelley, Reach & Lien 2008; Tubiana et al. 2008, 2011; Agarwal et al. 2010; Hadamcik et al. 2010; Tozzi et al. 2011; Lowry et al. 2012; Snodgrass et al. 2013, 2016; Vincent et al. 2013). Furthermore, useful collections of ground-based observations were published by Kidger (2004) and Ferrin (2005). The observational results represented valuable input information for the Rosetta mission planning. Since, for 67P, they cover different aspects of cometary properties and a wider and denser sampled time window than for many other JFCs, they allow also studies of the time evolution of the comet as well as new interpretations and insights on the background of the results evolving from the Rosetta mission.

Here, we present observations and results from the 2015/2016 return of comet 67P. The imaging observations focus on the coma structure and dust production versus time and try to link the results to the knowledge on the comet from previous apparition as well as to recent conclusions from the Rosetta data.

2 OBSERVATIONS AND DATA REDUCTION

The observations of 67P described here were performed at the Mt. Wendelstein Observatory (12°00′45″E, 47°42′13″N, 1837 m above sea level) of the University of Munich from 2015 August 22 to 2016 May 9, i.e. covering the period from 9 to 270 d after perihelion passage of the comet. In this period, the comet was imaged during 51 nights through Sloan Digital Sky Survey (SDSS; Fukugita et al.

⋆ E-mail: boehnhardt@mps.mpg.de

© 2016 The Authors
Published by Oxford University Press on behalf of the Royal Astronomical Society

Downloaded from https://academic.oup.com/mnras/article-abstract/462/Suppl_1/S376/2447817
by MPI Solar System Research user
on 03 September 2018

1996) r' filter using the Wendelstein Wide Field Imager (WWFI) camera (Gössl et al. 2012) at the 2 m Fraunhofer telescope (Hopp et al. 2014). During four nights, the comet was also imaged through SDSS filters g' and i'. The WWFI camera has a f/7.8 optics and is equipped with a CCD mosaic from Spectral Instruments, Tucson, mounting four 4 k × 4 k 15 μm 4-port read-out e2V CCDs that provides a pixel size of 0.2 arcsec and covers 27 arcmin × 27 arcmin on the sky. Information on the observing site and the technical equipment used can be found in Kosyra et al. (2014).

The Mt. Wendelstein imaging campaign of 67P covers the post-perihelion solar distance range of the comet from 1.248 to 2.966 au with Earth distances between 1.491 (2016 February 21) and 2.386 au (2016 May 9). During the campaign, the phase angle of the comet decreased first slowly from 33.9° at the beginning of the campaign to 29.3° on 2015 December 29, thereafter more rapidly to 4.0° on 2016 March 14 and increasing again after opposition to 17.8° at the end of the observing campaign. The pixel size of the camera resulted in projected extensions of 216.3 to 346.1 km at the comet. Table 1 provides the observing log of the 67P campaign at Mt. Wendelstein Observatory.

During the nightly observing window of the comet, image series of 67P were obtained with exposure times between a few 10 s (early phase of the campaign) up to 120 s (late phase) integration times, applying sidereal tracking and guiding to the telescope. The exposure times were chosen as such to freeze the cometary motion to the typical seeing of the site. Multiple consecutive images were taken each night for improvement of the signal-to-noise ratio and to allow us for the removal of background objects as well as artificial features (e.g. bad pixels, cosmics, inter-chip regions) in the images through post-processing of the data. For the latter reason, a fixed offset pattern (with 13 pointings) with a maximum amplitude of typically +/−120 arcsec was applied from image to image during the nightly exposure series. The offset pattern took care of keeping the coma and the tail region close to the comet head well-placed inside the camera field of view.

During the first weeks of the campaign, the cometary coma was imaged more frequently – basically during each useful night – in order to monitor possible short-term variability of the comet. Later on and based on the experience on the comet behaviour from the initial part of the campaign, the repetition cycle of the nightly images was also extended, to compensate for the decreasing object brightness by longer total integration times of the nightly series. Bias, dark current and sky flat-field exposures are available for the observing nights. Since flux calibration of the images is done via tabulated magnitudes of background stars in the individual exposures, no specific and dedicated photometric standard star fields were taken.

The data reduction was performed using a pipeline process developed and tuned at the University Observatory, Munich, specifically for the Mt. Wendelstein 2 m telescope and the WWFI camera. The raw images are subtracted by a monthly master bias in which two features are present: a time-stable vertical line pattern on a 0.02 ADU level and a - on time-scales of minutes - varying but uniform off-set level for each port of ∼400 ADU. This offset is determined from the three overscan regions of each of the 16 ports and subtracted. The dark current of the detectors is negligible at operational temperature of −115° C. Therefore, usually no dark exposures are subtracted. The images are thereafter divided by a daily master flat that is created from twilight sky flats. The large-scale pattern of the single sky flats is matched to one sky flat by the fourth-order polynomials to attain the same illumination before clipping stars and combining the calibrated sky images. Cosmic rays are effectively masked by the edge-detection routine from Gössl & Riffeser (2002). Charge persistence stripes are also masked. The bright regions commencing from saturated, bright stars along the vertical readout direction are contaminated for minutes to hours, depending on the intensity of saturation. The stripes are detected by comparing suspected areas to the local background and are then masked in subsequent exposures. Barely noticeable offsets between the ports remain after the basic data reduction. The offsets are adjusted to an average level by matching the background flux of 30 pixel wide stripes next to the port borders.

Next, the center of the comet was selected by visual inspection. In this step also, bad images, where the comet was contaminated by dead or masked columns, were removed. For the final images, the comet core was centred to a 1601 × 1601 pixels grid matching a size of 5.34 arcmin × 5.34 arcmin on the sky. In the last step, the images were photometrically aligned by their zero-point and the sky was subtracted.

The determination of the photometric zero-point in the individual images was adjusted to the Pan-STARRS-3 Pi source catalogue (PV3) in AB magnitudes (Magnier et al. 2013), which filter system, in turn, agrees well with SDSS AB magnitudes. Tonry et al. (2012) determined the conversions between the PS1 and SDSS filter system and indicate a small colour correction between PS1 and SDSS of 0.007*(g–r). Kosyra et al. (2014) measured the colour corrections between WWFI and SDSS to be 0.035*(r–i). Table 2 gives an overview of the bandwidth specifications of the filters used.

The differences for the r band are only marginal, i.e. the r SDSS filter is shifted in λ_{eff} about 4 nm to the red (at the flanks shifted less than 20 nm into the red), which may explain the small differences for the colour terms. Note, in particular, that all photometric data are reported in the SDSS system.

3 DATA POST-PROCESSING FOR THE ANALYSIS OF THE COMETARY IMAGES

From the flux-calibrated image series of a single night, the mean and the median-averaged composite frame is produced after proper centring of the individual frames to the central brightness peak in the coma. The typical centring accuracy is usually better than 0.2 pixels, i.e. below about 45–70 km at the distance of the comet. While the mean coma image contains all signatures from background objects as well as in parts from artificial and natural image artefacts, the median-averaged composite of a night (after photometric and sky alignment) is smoothed and widely cleaned from high signal levels of the background objects and image artefacts. However, it is noted that remnant signatures at the level of the local coma intensity level remain in the median composite images. Usually, no disturbing impact results from these contaminations for the further data analysis of the comet images. The averaged composite image of a single night provides the summary of the coma appearance of the nightly observing window, but it does not allow us to evaluate the temporal evolution of the coma during the nightly observing interval. Any such assessment requires the analysis of individual images of the night or subsets of them. The average composite images were removed from a minor sky background level remaining from the averaging process of the individual sky-removed images.

For the assessment of the cometary activity, further analysis methods are applied. The search for coma and tail structures starts with a visual inspection of the isophote pattern of the coma and tail for time variable and asymmetric patterns deviating from 'tear dropshape' coma isophotes. Furthermore, two structure enhancement methods are applied: (1) adaptive Laplace filtering (Boehnhardt

Downloaded from https://academic.oup.com/mnras/article-abstract/462/Suppl_1/S376/2447817
by MPI Solar System Research user
on 03 September 2018

Table 1. Observing log of the comet 67P observations at the Mt. Wendelstein Observatory. All observations were performed with the WWFI camera at the Fraunhofer 2 m-telescope. The table columns list the Modified Julian Date (MJD) and the civil observing date (UT), the observing time (UT), the Sun (r in au) and Earth (Δ in au) distance, the phase angle (°) of the comet, the pixel scale (km) at the distance of the comet, the exposure time used (s), the number of exposures taken, the total integration time on comet (s), the WFFI filter used and remarks.

MJD	Date (UT)	Time (UT)	r (au)	Δ (au)	Phase (°)	Pix. res. (km)	Exp. time (s)	Exp. number	Int. time (s)	WWFI Filter	Remarks
57256	2015/08/22	02:28–03:17	1.2482	1.7681	33.97	256.5	20.0	39	780	r	
57257	2015/08/23	02:27–03:08	1.2494	1.7681	33.97	256.5	20.0	36	720	r	
57261	2015/08/27	02:39–03:22	1.2552	1.7688	33.96	256.6	60.0	16	960	r	
57264	2015/08/30	02:33–03:18	1.2629	1.7705	33.94	256.8	20.0	35	700	r	
57265	2015/08/31	02:32–03:23	1.2629	1.7705	33.94	256.8	60.0	25	1500	r	
57275	2015/09/10	02:58–03:39	1.2900	1.7779	33.82	257.9	30.0	40	1200	r, g, i	02:58:03:25 for r 26 × 30 s, 03:25–03:30 for g 6 × 30 s, 03:31–03:39 for I 8 × 30 s
57277	2015/09/12	02:22–03:42	1.2967	1.7798	33.80	258.2	60.0	47	2820	r, g, I	02:22:03:04 for r 26 × 60 s, 03:10–03:29 for g 13 × 60 s, 03:29–03:42 for i 8 × 60 s
57278	2015/09/13	02:54–03:38	1.3003	1.7808	33.78	258.3	60.0	30	1800	r	
57283	2015/09/18	02:54–03:38	1.3233	1.7868	33.70	259.2	60.0	1	60	r	single exposure, bad seeing
57284	2015/09/19	03:25–03:57	1.3233	1.7868	33.70	259.2	60.0	18	1080	r	
57293	2015/09/28	03:49–04:13	1.3640	1.7959	33.59	260.5	60.0	16	960	r	
57294	2015/09/29	03:03–03:48	1.3689	1.7968	33.58	260.6	60.0	30	1800	r	
57295	2015/09/30	02:41–04:12	1.3739	1.7978	33.57	260.8	60.0	55	3300	r	
57296	2015/10/01	02:38–04:15	1.3790	1.7987	33.55	260.9	60.0	46	2760	r	
57297	2015/10/02	02:53–03:35	1.3842	1.7996	33.54	261.0	60.0	19	1140	r	
57305	2015/10/10	02:53–03:35	1.4282	1.8054	33.47	261.9	60.0	7	420	r	
57315	2015/10/20	02:53–03:44	1.4885	1.8087	33.40	262.4	60.0	31	1860	r	
57319	2015/10/24	02:59–04:42	1.5141	1.8084	33.38	262.3	60.0	54	3240	r	
57332	2015/10/25	02:47–02:49	1.5273	1.8079	33.36	262.2	60.0	1	60	r	single exposure
57321	2015/10/26	03:14–04:49	1.5273	1.8079	33.36	262.2	60.0	1	60	r	
57325	2015/10/30	03:52–04:31	1.5540	1.8060	33.32	262.0	60.0	25	1500	r	
57327	2015/11/01	03:13–04:52	1.5674	1.8047	33.30	261.8	60.0	52	3120	r	
57328	2015/11/02	03:33–04:53	1.5743	1.8039	33.29	261.7	60.0	48	2880	r	
57329	2015/11/03	03:28–05:00	1.5812	1.8031	33.28	261.5	60.0	59	3540	r	
57332	2015/11/06	01:52–02:34	1.6014	1.8001	33.24	261.1	60.0	27	1620	r	
57337	2015/11/11	03:49–05:10	1.6372	1.7934	33.16	260.1	60.0	52	3120	r	
57338	2015/11/12	03:48–05:02	1.6440	1.7919	33.14	259.9	60.0	48	2880	r	
57345	2015/11/19	03:42–04:00	1.6874	1.7809	32.99	258.3	60.0	12	720	r	bad seeing
57350	2015/11/24	03:18–04:12	1.7318	1.7670	32.77	256.3	60.0	36	2160	r	
57354	2015/11/28	04:04–04:25	1.7617	1.7561	32.58	254.7	60.0	14	840	r	
57362	2015/12/06	04:57–05:40	1.8148	1.7342	32.15	251.6	60.0	29	1740	r	
57377	2015/12/21	01:01–01:57	1.9358	1.6730	30.55	242.7	60.0	34	2040	r	
57381	2015/12/25	01:46–03.31	1.9670	1.6556	29.97	240.1	90.0	47	4230	r	
57382	2015/12/26	04:13–05:39	1.9753	1.6508	29.80	239.5	60.0	39	2340	r	
57383	2015/12/27	02:28–04:07	1.9825	1.6466	29.65	238.9	90.0	48	4320	r	
57385	2015/12/29	04:01–05:43	1.9985	1.6374	29.29	237.5	41.0	60	2460	r	
57387	2015/12/31	04:04–03:30	2.0140	1.6284	28.93	236.2	60.0	55	3300	r	
57409	2016/01/22	02:52–05:13	2.1833	1.5342	23.32	222.6	90.0	45	4050	r	
57410	2016/01/23	00:43–00:52	2.1899	1.5311	23.04	222.1	120.0	3	360	r	
57411	2016/01/24	00:55–05:45	2.1985	1.5271	22.66	221.5	70.0	120	8400	r	
57415	2016/01/27	04:12–05:18	2.2295	1.5139	21.22	219.6	120.0	15	1800	r	no useful data
57417	2016/01/30	03:43–05:31	2.2447	1.5081	20.48	218.8	120.0	30	3600	r, g, i	04:27:04:58 for r 10 × 120 s, 03:43–04:13 for g 10 × 120 s, 04:59–05:31 for i 10 × 120 s
57440	2016/02/21/22	21:41–01:54	2.4173	1.4910	10.48	216.3	120.0	23	2760	r	
57447	2016/02/28/29	23:47–00:28	2.4696	1.5097	7.27	219.0	120.0	13	1560	r	
57461	2016/03/14	20:23–22:46	2.5794	1.5950	3.99	231.4	120.0	39	4680	r	
57463	2016/03/16	19.54–22:04	2.5938	1.6111	4.38	233.7	120.0	39	4680	r	
57479	2016/04/01	21:39–23:45	2.7096	1.7820	9.72	258.5	120.0	39	4680	r	
57481	2016/04/03	20:05–20:52	2.7231	1.8067	10.35	262.1	120.0	15	1800	r	
57488	2016/04/10/11	22:01–00:16	2.7734	1.9060	12.53	276.5	120.0	37	4440	r	
57516	2016/05/07/08	19:59–00:25	2.9598	2.3678	17.76	343.5	120.0	45	5400	r, g, i	faint coma, 23:32–00:05 for r 15 × 120 s, 22:31–23:224 for g 15 × 120 s, 19:58–20:01 for i 15 × 120 s
57517	2016/05/08/09	22:33–00:19	2.9663	2.3862	17.86	346.1	120.0	30	3600	r	faint coma

Downloaded from https://academic.oup.com/mnras/article-abstract/462/Suppl_1/S376/2447817
by MPI Solar System Research user
on 03 September 2018

Table 2. Passband parameters of the *g*, *r*, *i* filters for WWFI, PS1 and SDSS.

	$\lambda_{\rm eff}$ (nm)	$\lambda_{\rm blue}$ (nm)	$\lambda_{\rm red}$ (nm)
g band			
WWFI	480.3	418	550
PS1	483.2	414	552
SDSS	476.6	411	561
r band			
WWFI	619.3	557	695
PS1	618.8	548	694
SDSS	622.7	563	713
i band			
WWFI	758.6	698	836
PS1	752.5	688	824
SDSS	764.2	699	869

& Birkle 1994) using different filtering width for narrow (7 pixels wide) to extended (128 pixels wide) features and (2) coma renormalization (A'Hearn et al. 1986) by either dividing or subtracting a two-dimensional (2D) coma profile created from the mean radial coma profile obtained from the comet image. For the latter, the original and the 2D-profile image are aligned to each other via the central brightness peaks in the coma. While the adaptive Laplace filtering is very sensitive to low-level systematic local and global brightness differences in the coma and tail region, it reduces the effective spatial resolution of the noticeable structures in the image according to the filter width chosen. Moreover, in our application, it introduces a non-linear scaling of the enhanced structure such that only geometric, but no quantitative photometric conclusions can be obtained. The renormalization method is less sensitive to low-level structures, but keeps the linear intensity scaling of the result image as well as it does not reduce the geometric resolution of the result frame. However, artefacts (artificial structures) can result from decentring between the original and the 2D-profile image, in particular, close to the coma center. Coma and tail structures found by either one of the enhancement methods described above need to be verified, ideally, by the respective alternative method and in any case by an inspection of the original image for systematic irregularities in its isophote pattern. The two enhancement methods are applied to all individual exposures of the comet as well as to the mean- and median-averaged composite frames of the individual nights. Inspections of the time series of processed individual images are used for an assessment of short-term variability of coma structures identified. The mean- and median-averaged composites provide a much higher signal to noise for an extended and quantitative assessment of the coma, in particular, also for the extended geometry of coma features. Fig. 1 shows an example of a composite image of 67P processed by the enhancement methods described above.

For the assessment of the global coma status, radial profiles of the median-averaged composite images of the individual nights are considered. The radial profiles are obtained by flux integration in concentric rings of increasing radius centred on the central brightness peak in the coma. The gradient slope in the average radial profile is approximated in a linear fit to the log–log pairs for the flux versus the distance in the coma. Different distance ranges, 5000–10 000, 10 000–15 000, 15 000–20 000 and 20 000–25 000 km are used for the slope fitting. The different ranges allow for the assessment of possible changes in the slope parameter with radial distance from the nucleus, originating from, for instance, radiation pressure effects on the coma dust, gas contamination in the broad-band filter images and physical changes of the coma content.

4 RESULTS

Comet 67P displayed an extended coma over the whole observing interval from 2015 August 22 (1.24 au post-perihelion) until the end of the observations on 2016 May 9 (2.97 au post-perihelion). A direct signature of the cometary nucleus is not detected. It is assumed to be hidden in the central brightness peak of the coma produced by the atmospheric seeing. Thus, the nucleus may still contribute to the total brightness of the coma measured in circular apertures centred on the central brightness peak. The available images and measured data allow us to characterize the cometary activity and properties of the coma, i.e. the magnitude, colours and spectral slopes, radial coma profiles, dust activity, coma structures and tail appearance.

Coma magnitudes*:* in the *r*-filter images, the coma magnitude was measured centred on the nucleus position for four aperture radii, i.e. for 5000, 10 000, 15 000 and 20 000 km at the distance of the comet (Fig. 2, Table 3). Maximum brightness of the comet is found for the period of 2015 late August to early September. Since the observations start only 9 d after perihelion, the period of maximum brightness is not well-constrained from our data. Between about 2015 late September and at least to the end of December, the coma magnitude followed a decrease, approximately linearly with time. As of the last third of 2016 January, the comet displayed a close to constant coma magnitude in the measured apertures until the end of 2016 February when it started to get fainter again. Typical measurement errors are in the range 0.03–0.05 mag, except for a few nights with bad seeing and when the coma got very faint in 2016 May (errors ∼0.1 mag). Variable coma brightness during the nightly exposure window beyond the uncertainty range for the individual nights is not found for the four aperture sizes used. Variations over several nights are generally slow as well as of small amplitude and they appear to be associated with the long-term activity evolution of the comet. Brightness enhancements beyond 0.2 mag, indicating a short-term outburst of the comet, are not identified in our observations.

Coma colours*:* the colour of the coma dust is calculated from the flux-calibrated images of 67P and is obtained for four observing epoch, each using three pairs of filters (*g*-*r*, *r*-*i* and *g*–*i*), i.e. for 2015 September 10 and 12, 2016 January 30 and 2016 May 7/8 (see Table 4). Using the central wavelengths of the filters as a reference, the equivalent average spectral slope *S* can be estimated for the wavelength range covered by the filters (see Table 2) using formula (1)

$$S = \left[10^{(-0.4*(C_{\rm comet} - C_{\rm sun}))}\right] / [\lambda_{\rm long} - \lambda_{\rm short}], \qquad (1)$$

with $C_{\rm comet}$ and $C_{\rm sun}$ as the magnitude differences of the comet and Sun, respectively, measured for the filter pair with effective central wavelengths $\lambda_{\rm long}$ and $\lambda_{\rm short}$.

Due to the larger solar distance (2.24 and 2.96 au), the gas emission in the 67P coma in the *g*-, *r*-, *i*-filter ranges should be negligibly low on 2016 January 30 and May 7/8, such that the measured colours and estimated spectral slopes can be considered to represent the values of the cometary dust. At that time (phase angle of the comet was 20.5° and 17.8°, respectively) the reddening of the dust coma was about 12 per cent/100 nm in *g*–*r* wavelength range, about 8.5 per cent/100 nm for *r*–*i* and about 11 per cent/100 nm for *g*–*i*. The dust reddening of 67P is slightly decreasing with increasing wavelength, a phenomenon seen, for instance, for the surface of 67P

Downloaded from https://academic.oup.com/mnras/article-abstract/462/Suppl_1/S376/2447817
by MPI Solar System Research user
on 03 September 2018

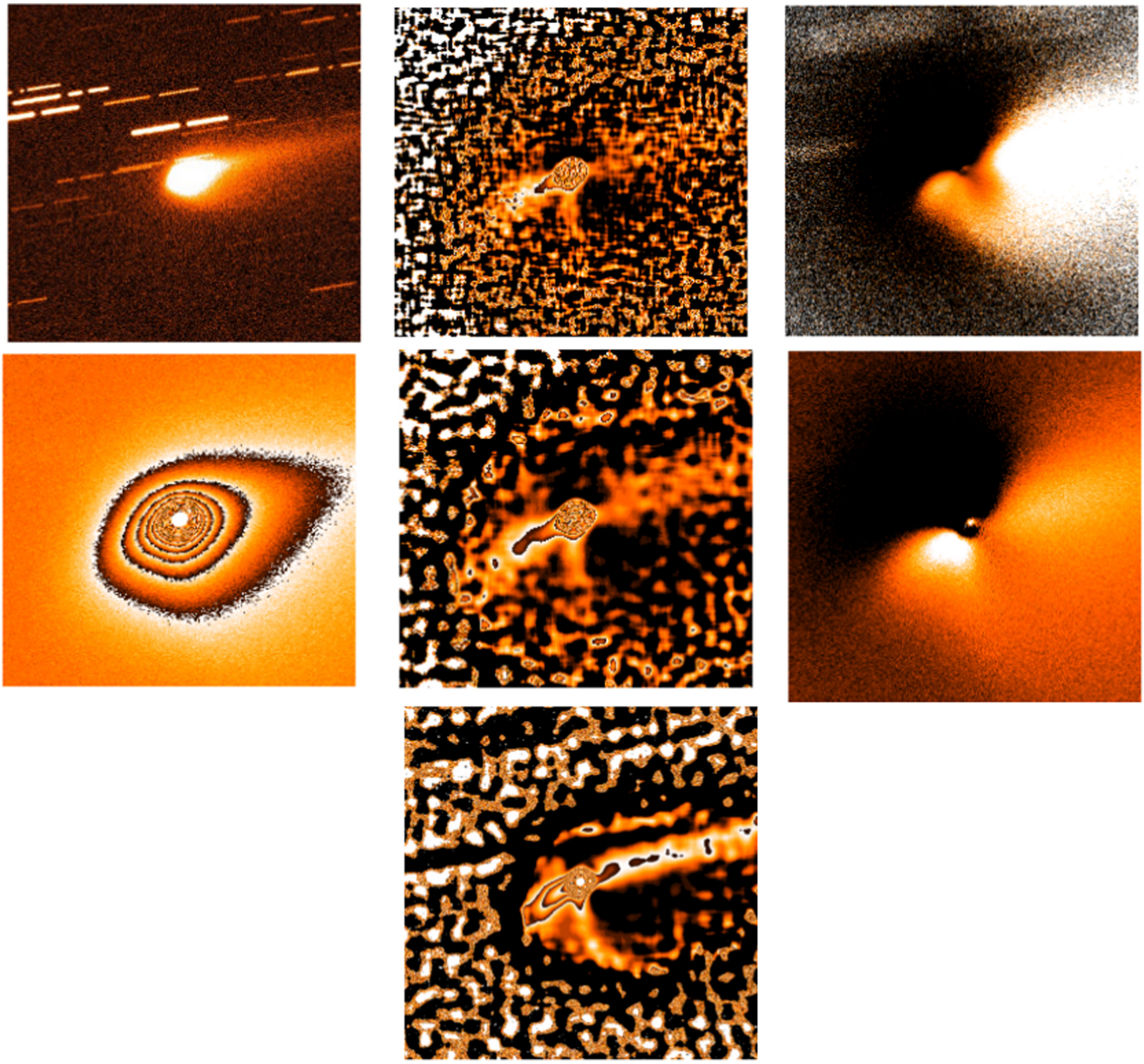

Figure 1. Example images from the structure enhancement processing of 67P from the night on 2015 September 10. The images show: left-hand column – top panel: the full frame composite of the comet (290 000 × 290 000 km); Bottom panel: isophote pattern of the cometary coma (65 000 × 65 000 km). Middle column – top panel: Laplace-filtered image of the coma, filter width with 15 pixels (65 000 × 65 000 km); Middle panel: Laplace-filtered image of the coma, filter width 23 pixels (65 000 × 65 000 km); Bottom panel: Laplace-filtered image of the coma, filter width 47 pixels (130 000 × 130 000 km); Right-hand column, top panel: renormalized image, ratio of original by average coma profile (65 000 × 65 000 km); Bottom panel: renormalized image, difference between original and average coma profile (65 000 × 65 000 km). The listed distances describe the field of view at the distance of the comet. Image orientation is north up, east to the left.

(Fornasier et al. 2015), other cometary nuclei (Lamy et al. 2004) and Kuiper Belt objects (Doressoundiram et al. 2007). Within the measurement uncertainties, these values also agree with the colours and spectral gradients determined for the nucleus of 67P by Tubiana et al. (2008, 2011) and Lowry et al. (2006). It is slightly below the spectral slope determined from *in situ* measurements of dust grains in the coma of 67P (Cremonese et al. 2015). No clear increase of the reddening with phase angle is seen in our data. Although at the detection limit, there might be increasing and decreasing trends in the coma colours and spectral slopes with increasing distance in the coma. In 2D colour images, no reddening variations could be identified that can be associated with the coma structures (described below).

The mean *g*–*r* and *g*–*i* colours and spectral slopes are lower on 2015 September 10 and 12 than in 2016 January and May, while the *r*–*i* colours seem to agree within the errors for all four observing epochs. This is taken as indication that gas emission, i.e. mostly from C_2 molecules, is contributing significantly to the measured coma flux in the *g* filter on 2015 September 10 and 12, when the comet had passed perihelion for about a month (solar distance of about 1.3 au). The agreement of the *r*–*i* colours and spectral slopes for all four observing epochs with the comet at

Downloaded from https://academic.oup.com/mnras/article-abstract/462/Suppl_1/S376/2447817
by MPI Solar System Research user
on 03 September 2018

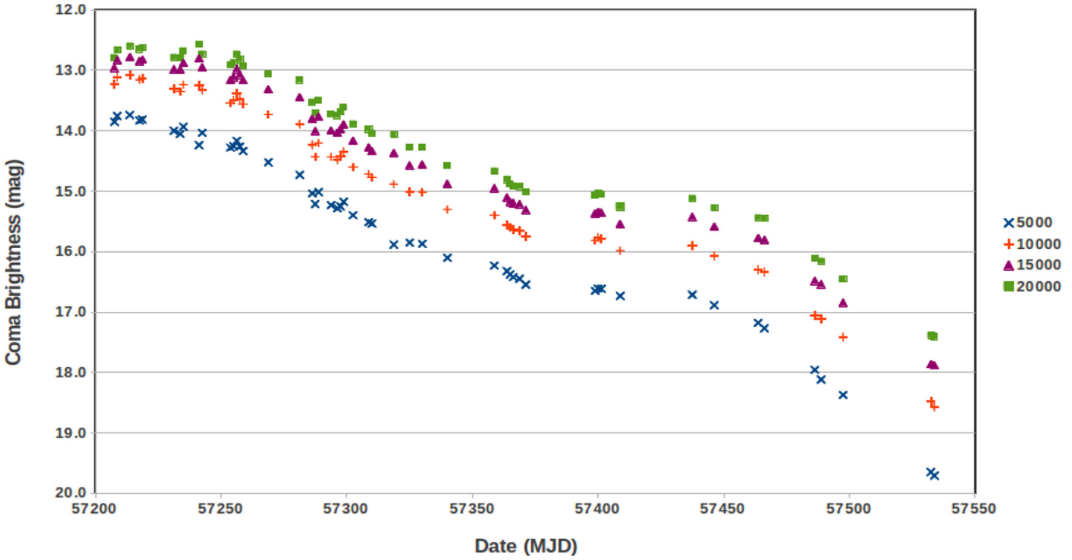

Figure 2. Coma magnitude of 67P/Churyumov–Gerasimenko, measured in the WWFI *r* filter, versus time. The results for four different projected aperture radii at the distance of the comet (5000, 10 000, 15 000, 20 000 km) are plotted. The time is given as Modified Julian Date (MJD).

1.3, 2.2 and 2.9 au, respectively, is seen as an argument to assume that the *r*–*i* wavelength region is not significantly contaminated by gas emissions and thus represents the comet appearance in dust-reflected sunlight. Possible weak gas contamination in this spectral range could come from C_2, NH_2 molecules and the [O I] line in the coma, but is usually not noticeable in the images of comets taken with broad-band filters in the red wavelength region.

Dust activity*:* the dust activity of comets is typically characterized by determining the afρ parameter of the coma in a wavelength region where dust-reflected sunlight dominates the coma brightness. The afρ approach for the characterization of the dust activity of comets was introduced by A'Hearn, Millis & Thompson (1984) and provides a quantitative equation that connects the projected aperture radius ρ at the distance of the comet, the so-called filling factor *f* of the cometary dust in the light path and the albedo *a* of the dust (which is assumed to be constant for all reflecting dust grains) with the measured coma flux.

$$\mathrm{af}\rho = 4^{*}\Delta^{2^{*}}r^{2}/\rho^{*}\, f_{\mathrm{comet}}/f_{\mathrm{sun}}. \tag{2}$$

In equation (2), Δ and *r* denote the Earth and Sun distance of the comet, respectively, and f_{comet} and f_{sun} are the fluxes of the comet and Sun, respectively, in the filter band used for the measurements. Note that for a 'quasi-steady-state' coma with homogeneous and isotropic dust expansion, constant production level of the nucleus for the dust in the measurement aperture, and neglecting changes of the dust properties due to radiation pressure effects along their travel through the measurement aperture, the afρ parameter should be independent from the size of the measurement aperture.

For the estimation of the light contribution of the 67P nucleus to the total brightness measured in circular apertures centred on the central brightness peak in the coma, we applied the standard formulas (equations 3 and 5 in Lamy et al. 2004) and the values for the equivalent radius (1.98 km; Lamy et al. 2008), albedo (0.059; Sierks et al. 2015) and linear phase darkening (0.04 mag deg^{-1}; Snodgrass et al. 2013). The parameters used for the nucleus light calculations are to be seen as approximation only, since an accurate prediction of the nucleus brightness (considering shape, rotation, surface reflectivity and light scattering geometry) is not available.

Fig. 3 shows the results for different aperture radii: for the largest aperture used (20 000 km radius), the nucleus contribution is below 1 per cent until 2015 mid-November and does not exceed 7 per cent by 2016 early May. The smallest aperture (5000 km radius) receives less than 2 per cent of nucleus light until about 2015 mid-October, but has a high contribution of more than 50 per cent towards the end of the Wendelstein observations of 67P. For the 10 000 km radius aperture – which is considered a good reference for comparison with other publications – the level of 5 per cent nucleus light contribution was reached in 2016 January.

As argued from the colour measurements for 67P, the best – since widely free of gas contamination – wavelength region for assessing the dust activity are in the WWFI *r*- and *i*-filter pass bands. Because of the large number of data available, we thus use the *r*-filter images for determining the afρ values of 67P over time, again applying aperture radii of 5000, 10 000, 15 000 and 20 000 km at the distance of the comet (see Table 3). Fig. 4 shows the evolution of afρ versus time, derived directly from the WWFI *r*-filter brightnesses of the comet.

After a plateau during 2015 late August that represents the likely maximum activity level mentioned above, the dust activity of 67P decreased almost linearly with time until at least the end of 2015 December. As of 2016 late January, a bump is noticeable in the afρ evolution lasting until at least 2016 early April. During 2015 late September, until 2016 January, the afρ curves for different aperture radii in the cometary coma show only minor differences. This indicates that the dust coma was in 'quasi-steady-state' very close to the assumption made for the afρ assessment via equation (3). During this time interval, a small trend of decreasing afρ values with increasing aperture size during a single measurement epoch is seen for 67P. During 2015 late August until mid-September and as of 2016 February, the afρ values for the four aperture radii spread further apart in a systematic manner, i.e. during the earlier period, the afρ values for smaller aperture radii are higher and vice versa during the latter time period. This indicates that the dust coma of the comet was not in 'quasi-steady-state' and is discussed further below.

Fig. 4 suggests that the dust production represented by the afρ measurements follows approximately an exponential law with

Downloaded from https://academic.oup.com/mnras/article-abstract/462/Suppl_1/S376/2447817
by MPI Solar System Research user
on 03 September 2018

Table 3. Radial gradient, magnitude and afρ parameter of the dust coma of 67P during the observing period. The table lists the Modified Julian Date (MJD) and UT date of the observation, the Sun (r in au) and Earth (Δ in au) distance of the comet, its phase angle (deg) and the slope, magnitude (mag) and afρ parameter of the dust coma. The latter three quantities are listed for four distance ranges (5000/10 000, 10 000/15 000, 15 000/20 000, 20 000/25 000 km) and four aperture radii (5000, 10 000, 15 000, 20 000 km). NM means not measured or calculated. The uncertainty of magnitude measurements is mostly about 0.03–0.05 mag, that of the radial slope is about 0.02.

67P MJD	**Dust Coma** Date (UT)	r (au)	Δ (au)	Phase (deg)	Slope 5000/ 10000 km	Slope 10000/ 15000 km	Slope 15000/ 20000 km	Slope 20000/ 25000 km	Magnitude 5000 km	Magnitude 10000 km	Magnitude 15000 km	Magnitude 20000 km	Afρ (cm) 5000 km	Afρ (cm) 10000 km	Afρ (cm) 15000 km	Afρ (cm) 20000 km
57256	20150822	1.2482	1.7681	33.97	0.79	0.62	0.52	0.46	13.85	13.23	12.96	12.79	369	327	280	246
57257	20150823	1.2494	1.7681	33.97	0.82	0.64	0.51	0.44	13.76	13.11	12.83	12.67	404	366	316	276
57261	20150827	1.2552	1.7688	33.96	0.84	0.68	0.57	0.50	13.74	13.08	12.78	12.60	415	383	334	297
57264	20150830	1.2629	1.7705	33.94	0.86	0.73	0.65	0.62	13.83	13.16	12.85	12.65	387	359	318	287
57265	20150831	1.2629	1.7705	33.94	0.87	0.71	0.62	0.56	13.82	13.13	12.83	12.63	393	368	325	293
57275	20150910	1.2900	1.7779	33.82	1.03	1.01	0.96	0.93	14.00	13.31	12.98	12.79	348	330	296	266
57277	20150912	1.2967	1.7798	33.80	0.93	0.77	0.65	0.56	14.05	13.35	12.99	12.79	336	321	297	268
57278	20150913	1.3003	1.7808	33.78	0.92	0.77	0.66	0.58	13.93	13.24	12.88	12.68	377	358	331	300
57283	20150918	1.3233	1.7868	33.70	1.30	0.94	0.76	0.64	14.24	13.25	12.81	12.57	295	368	368	343
57284	20150919	1.3233	1.7868	33.70	0.93	0.81	0.78	0.71	14.04	13.33	12.95	12.73	358	344	325	298
57293	20150928	1.3640	1.7959	33.59	0.95	0.84	0.74	0.68	14.28	13.54	13.16	12.91	308	303	287	271
57294	20150929	1.3689	1.7968	33.58	1.01	0.89	0.78	0.71	14.26	13.50	13.11	12.87	317	318	303	283
57295	20150930	1.3739	1.7978	33.57	1.03	0.89	0.77	0.68	14.17	13.38	12.98	12.73	347	359	345	325
57296	20151001	1.3790	1.7987	33.55	1.03	0.89	0.79	0.71	14.26	13.47	13.07	12.82	321	331	319	301
57297	20151002	1.3842	1.7996	33.54	1.02	0.89	0.78	0.68	14.34	13.56	13.17	12.92	302	308	295	277
57305	20151010	1.4282	1.8054	33.47	1.06	0.98	0.89	0.84	14.52	13.73	13.32	13.06	272	281	275	263
57315	20151020	1.4885	1.8087	33.40	1.11	1.01	0.91	0.81	14.73	13.89	13.45	13.16	245	266	266	260
57319	20151024	1.5141	1.8084	33.38	1.06	0.99	0.88	0.77	15.04	14.24	13.80	13.53	191	200	198	192
57332	20151025	1.5273	1.8079	33.36	1.05	0.99	0.94	0.84	15.21	14.43	14.01	13.71	164	168	166	164
57321	20151026	1.5273	1.8079	33.36	1.07	0.99	0.89	0.77	15.01	14.21	13.77	13.49	198	209	208	201
57325	20151030	1.5540	1.8060	33.32	1.06	0.99	0.88	0.77	15.23	14.44	14.00	13.72	168	175	174	168
57327	20151101	1.5674	1.8047	33.30	1.07	1.00	0.90	0.79	15.28	14.48	14.03	13.75	163	171	171	167
57328	20151102	1.5743	1.8039	33.29	1.10	1.01	0.91	0.80	15.25	14.42	13.97	13.69	168	181	183	178
57329	20151103	1.5812	1.8031	33.28	1.11	1.01	0.91	0.80	15.18	14.34	13.90	13.61	182	196	198	193
57332	20151106	1.6014	1.8001	33.24	1.06	1.01	0.92	0.81	15.40	14.60	14.17	13.89	152	158	157	153
57337	20151111	1.6372	1.7934	33.16	1.06	1.01	0.92	0.81	15.52	14.72	14.28	13.98	141	147	148	146
57338	20151112	1.6440	1.7919	33.14	1.02	0.98	0.90	0.80	15.54	14.77	14.34	14.04	140	141	141	139
57345	20151119	1.6874	1.7809	32.99	1.32	1.11	0.98	0.89	15.88	14.88	14.37	14.07	106	132	142	141
57350	20151124	1.7318	1.7670	32.77	1.07	1.02	0.93	0.84	15.85	15.01	14.58	14.28	113	122	122	120
57354	20151128	1.7617	1.7561	32.58	1.09	1.01	0.93	0.84	15.87	15.02	14.56	14.28	113	124	126	123
57362	20151206	1.8148	1.7342	32.15	1.06	1.01	0.95	0.85	16.10	15.31	14.88	14.58	94	98	97	96
57377	20151221	1.9358	1.6730	30.55	1.06	0.99	0.93	0.87	16.23	15.40	14.95	14.67	89	96	96	94
57381	20151225	1.9670	1.6556	29.97	1.05	1.00	0.93	0.85	16.32	15.56	15.11	14.81	83	84	85	83
57382	20151226	1.9753	1.6508	29.80	1.04	0.99	0.93	0.88	16.38	15.60	15.18	14.88	79	81	79	78
57383	20151227	1.9825	1.6466	29.65	1.05	1.00	0.95	0.89	16.42	15.64	15.20	14.91	76	78	78	76
57385	20151229	1.9985	1.6374	29.29	1.05	1.00	0.93	0.83	16.45	15.66	15.22	14.92	74	77	77	76
57387	20151231	2.0140	1.6284	28.93	1.06	1.00	0.94	0.88	16.55	15.75	15.31	15.02	68	71	71	70
57409	20160122	2.1833	1.5342	23.32	1.07	1.03	0.94	0.90	16.65	15.82	15.37	15.07	65	70	70	69
57410	20160123	2.1899	1.5311	23.04	1.05	0.99	0.91	0.81	16.61	15.77	15.35	15.04	67	73	72	72

Downloaded from https://academic.oup.com/mnras/article-abstract/462/Suppl_1/S376/2447817
by MPI Solar System Research user
on 03 September 2018

Table 3 – *continued*

67P MJD	**Dust Coma** Date (UT)	r (au)	Δ (au)	Phase (deg)	Slope 5000/ 10000 km	Slope 10000/ 15000 km	Slope 15000/ 20000 km	Slope 20000/ 25000 km	Magnitude 5000 km	Magnitude 10000 km	Magnitude 15000 km	Magnitude 20000 km	Afρ (cm) 5000 km	Afρ (cm) 10000 km	Afρ (cm) 15000 km	Afρ (cm) 20000 km
57411	20160124	2.1985	1.5271	22.66	1.07	1.00	0.94	0.88	16.62	15.79	15.35	15.05	67	72	72	71
57415	20160127	2.2295	1.5139	21.22	NM	NM	NM	NM	NM	NM	NM	NM	NM	NM	NM	NM
57417	20160130	2.2447	1.5081	20.48	1.03	0.99	0.94	0.91	16.73	15.99	15.54	15.26	61	61	61	60
57440	20160221/22	2.4173	1.4910	10.48	1.08	1.08	1.07	1.04	16.71	15.90	15.43	15.12	71	75	77	77
57447	20160228/29	2.4696	1.5097	7.27	1.12	1.08	1.02	0.97	16.89	16.07	15.59	15.28	64	68	71	71
57461	20160314	2.5794	1.5950	3.99	1.14	1.16	1.09	1.03	17.18	16.30	15.78	15.44	60	68	73	74
57463	20160316	2.5938	1.6111	4.38	1.18	1.19	1.13	1.05	17.27	16.34	15.81	15.45	57	67	73	76
57479	20160401	2.7096	1.7820	9.72	1.21	1.25	1.20	1.12	17.96	17.06	16.48	16.11	40	46	52	55
57481	20160403	2.7231	1.8067	10.35	1.36	1.28	1.25	1.30	18.12	17.11	16.54	16.16	36	46	51	55
57488	20160410/11	2.7734	1.9060	12.53	1.26	1.28	1.25	1.17	18.37	17.41	16.85	16.45	33	40	45	48
57516	20160507/08	2.9598	2.3678	17.76	1.45	1.44	1.45	1.33	19.65	18.48	17.86	17.39	18	26	31	36
57517	20160508/09	2.9663	2.3862	17.86	1.45	1.66	1.49	1.31	19.71	18.57	17.88	17.41	17	25	31	36

solar distance r, i.e. afr $\sim r^{\gamma}$. The radial exponent γ is obtained by a least-square fit to the afρ data for the time interval of the 'quasi-steady-state' dust coma, i.e. from 2015 September 27 to December 30. The results for the heliocentric exponent of the dust activity decrease of 67P are listed in Table 5 for the 10 000 km radius reference aperture. Other aperture radii (5000, 15 000, 20 000 km) give very similar results within the uncertainties of the fits.

In order to assess the impact of the brightness enhancement due to the phase function effects in the light scattering of the coma dust, we apply different phase function corrections to the measured coma brightness of 67P for the 10 000 km aperture radius. In general, the phase function reduces the reflected coma magnitude value. For small phase angles α (typically up to 30°), a linear reduction with α can be applied with typical parameters β for comets between 0.02 and 0.06 (Lamy et al. 2004). Alternatively, the two-parameter phase function of Schleicher, Millis & Birch (1998), based on 1P/Halley measurements, is available or the phase angle correction by Müller (1999) that also considers geometric projection effects by a non-spherical coma, symmetric to the radial direction with respect to the Sun. Fornasier et al. (2015) obtained results for the 67P nucleus surface reflectivity applying a HG-type phase function (Bowell et al. 1989) with a best-fitting G of −0.13. Fig. 5 shows the phase angle-corrected afρ values of 67P for the various phase function solutions. In Fig. 5, $\beta = 0.04$ is used as mean value for the linear phase function that is lower than the β value found for the nucleus of 67P (0.059–0.076; Tubiana et al. 2011; Lowry et al. 2012). A second HG-type phase function is applied as well with $G = 0.15$ that is found from many asteroid light curves (Tedesco 1989). Obviously, the afρ value for zero phase angle depends on the phase darkening and is highest for the Bowell-type phase function with $G = -0.13$ (as obtained for the 67P nucleus by Fornasier et al. 2015). Two phase functions provide a close to linear decrease of afρ with solar distance over the time interval from the end of 2015 September to the beginning of 2016 April, i.e. the linear phase function with $\beta = 0.04$ and the Bowell-HG-type phase function with $G = 0.15$. The phase functions of Schleicher et al. (1998) and of Müller (1999) can approximate the afρ data well between the end of September and end of December, but do not describe well the 67P dust activity measured in 2016.

The dust activity of 67P after 2015 mid-September until 2016 early May can be described as an exponential decrease by adopting either a linear phase function with $\beta \sim 0.04$ or a HG-type phase function with $G \sim 0.15$. Phase function corrections after Schleicher and Müller require deviating dust activity around the time of opposition passage of 67P (2016 January to April), while the HG-type phase corrections of Fornasier et al. results in a small drop of the dust activity around that time period. Based on our observation, a continuous exponential decrease of afρ with increasing heliocentric distance appears to be likely, since there is no clear evidence for an enhanced activity in the light curve for the 2016 opposition passage of 67P.

The exponent for the heliocentric activity decrease fitted to our observations from 2015 September 27 to December 30 are listed in Table 5. They vary depending on the adopted phase function approximation between about −3.7 and −4.2. Considering nucleus brightness contributions in the aperture measurements will change the heliocentric afρ exponent by −0.1. Different authors (A'Hearn et al. 1995; Kidger 2004; Schleicher 2006; Agarwal, Müller & Grün 2007) found a wide range of exponent values for the afρ decrease of 67P post-perihelion, i.e. from $\gamma = -0.4$ to -9.5. Our γ exponent values for a likely continuous dust activity decrease are −4.1 to −4.2 (for the linear – $\beta = 0.04$ - and HG-type phase functions – $G = 0.15$), which is considerably steeper than the one of Snodgrass

Downloaded from https://academic.oup.com/mnras/article-abstract/462/Suppl_1/S376/2447817
by MPI Solar System Research user
on 03 September 2018

Table 4. Filter colours and average spectral slope of the 67P coma for different aperture sizes. Filter colours and spectral slopes are given for the WWFI *g*, *r*, *i* filters and for four coma aperture radii (5000, 10 000, 15 000, 20 000 km) as well as the mean values of the results for the aperture radii. Solar colours used are 0.44 mag for *g*–*r*, 0.11 mag for *r*–*i* and 0.55 mag for *g*–*i*. The larger scatter of the results for 2016 May 7/8 is due to the higher uncertainties in the coma photometry because of the very much reduced cometary brightness.

Filter Range Coma radius (km)	*g*–*r* 5000	*g*–*r* 10 000	*g*–*r* 15 000	*g*–*r* 20 000	*g*–*r* mean	*r*–*i* 5000	*r*–*i* 10 000	*r*–*i* 15 000	*r*–*i* 20 000	*r*–*i* mean	*g*–*i* 5000	*g*–*i* 10 000	*g*–*i* 15 000	*g*–*i* 20 000	*g*–*i* mean	
201/509/10	0.59	0.56	0.53	0.50	0.55	0.22	0.22	0.21	0.21	0.22	0.81	0.78	0.75	0.71	0.76	Colour
	10.5	8.4	6.4	4.3	7.4	7.9	7.7	7.1	6.7	7.4	9.8	8.5	7.1	5.7	7.8	Spectral gradient
2015/09/12	0.58	0.57	0.54	0.51	0.55	0.25	0.23	0.23	0.22	0.23	0.83	0.80	0.76	0.73	0.78	Colour
	9.9	8.8	6.7	4.6	7.5	10.2	8.5	8.0	7.6	8.6	10.7	9.2	7.7	6.3	8.5	Spectral gradient
2016/01/30	0.62	0.61	0.61	0.61	0.61	0.22	0.23	0.24	0.25	0.23	0.84	0.84	0.85	0.86	0.85	Colour
	12.9	12.6	12.4	12.2	12.5	7.7	8.2	9.0	9.6	8.6	11.0	11.1	11.5	11.7	11.3	Spectral gradient
2016/05/07	0.48	0.62	0.64	0.67	0.60	0.35	0.24	0.18	0.14	0.23	0.82	0.85	0.82	0.82	0.83	Colour
	2.4	12.7	14.5	17.2	11.7	17.5	8.9	4.6	2.2	8.3	10.3	11.6	10.0	10.0	10.5	Spectral gradient

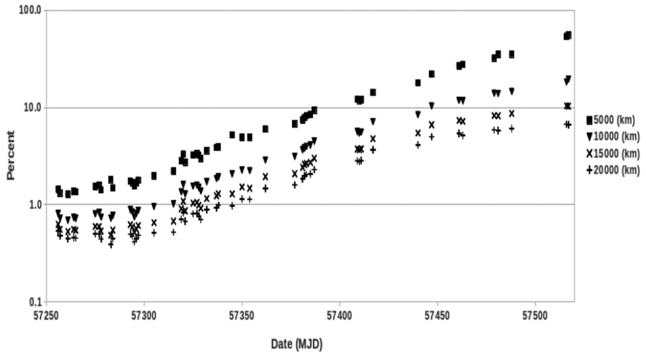

Figure 3. Estimated percentage of nucleus brightness to the total cometary brightness for different measurement aperture radii (5000, 10 000, 15 000, 20 000 km). The ratio is plotted over the full period of the Mt. Wendelstein observations of the comet.

Table 5. Heliocentric distance exponent for the afρ decrease of the coma of 67P. The table lists for the various phase function models the best-fitting exponent γ to the afρ data in a 10 000 km radius aperture for the time interval 2015 September 27–December 30. Phase functions used are 'none', 'linear', 'Schleicher', 'Müller', 'Fornasier' and 'Bowell', as described in the text.

Phase correction	Dust activity exponent (incl. nucleus)	Dust activity exponent (excl. nucleus)
None	−3.79 +/− 0.13	−3.88 +/− 0.13
Linear	−4.19 +/− 0.12	−4.27 +/− 0.12
Schleicher	−3.73 +/− 0.14	−3.82 +/− 0.14
Müller	−3.80 +/− 0.13	−3.89 +/− 0.13
Fornasier	−4.21 +/− 0.12	−4.30 +/− 0.12
Bowell	−4.07 +/− 0.13	−4.16 +/− 0.13

et al. (2013) with $\gamma \sim -3.4$. It is noted that phase reddening effects of the 67P dust are not obvious from our observations (see Table 4), although our colour data represent essentially only three epochs (2015 September 10 + 12, 2016 January 29 and 2016 May 7/8) with a phase angle difference of about 25°.

Additional indications for enhanced or reduced dust activity in 67P during the first quarter of 2016 do not exist in our data. Instead, the afρ level in 2016 early May is in-line with a continuous drop in dust activity of 67P following the behaviour as

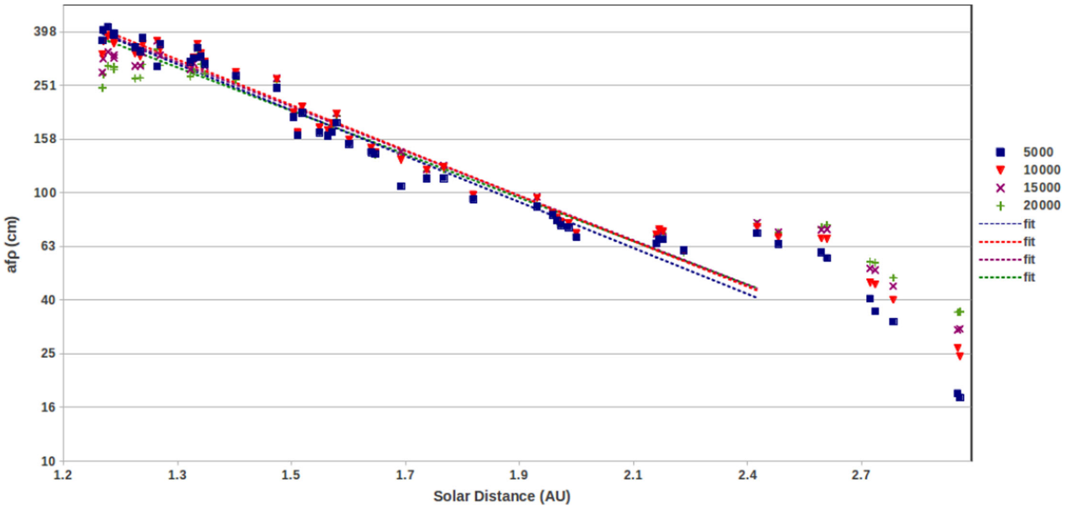

Figure 4. Evolution of the dust activity of 67P: afρ versus solar distance (au). The afρ parameter, determined from *r*-filter images, is plotted for four measurement aperture radii (5000, 10 000, 15 000, 20 000 km). *y*-axis (afρ) is logarithmic, *x*-axis (solar distance) is linear. The broken lines in the lower panel represent the best-fitting results for the observed afρ versus solar distance for the four aperture radii. The fit is performed for measurements from 2015 September 27 to December 30.

Downloaded from https://academic.oup.com/mnras/article-abstract/462/Suppl_1/S376/2447817
by MPI Solar System Research user
on 03 September 2018

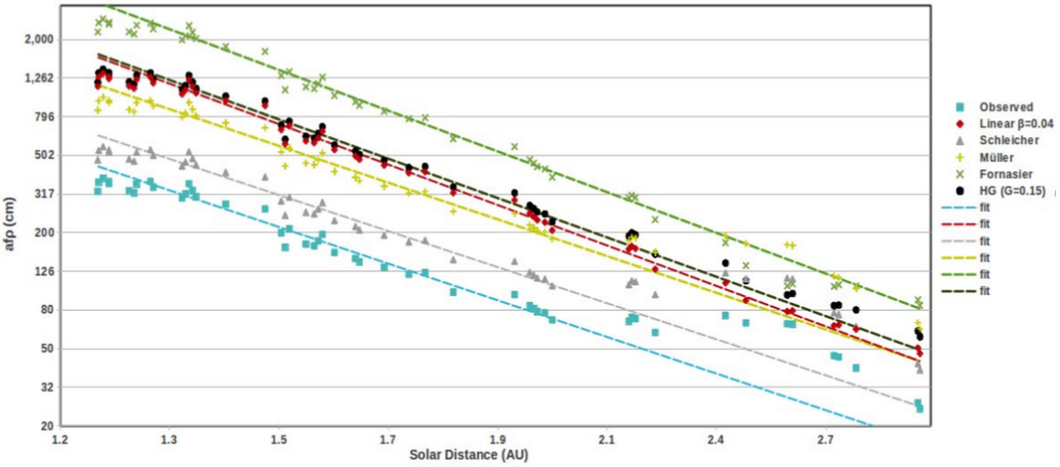

Figure 5. Dust parameter afρ of 67P versus solar distance, corrected for the different phase functions. The dashed lines indicate the best-fitting solutions for the power law of the various phase function-corrected afρ curves versus solar distance. All afρ values refer to coma brightness measurements of 67P through a 10 000 km radius aperture. Symbols and dashed lines represent the measured and best-fitting values of afρ for the respective phase functions corrected data.

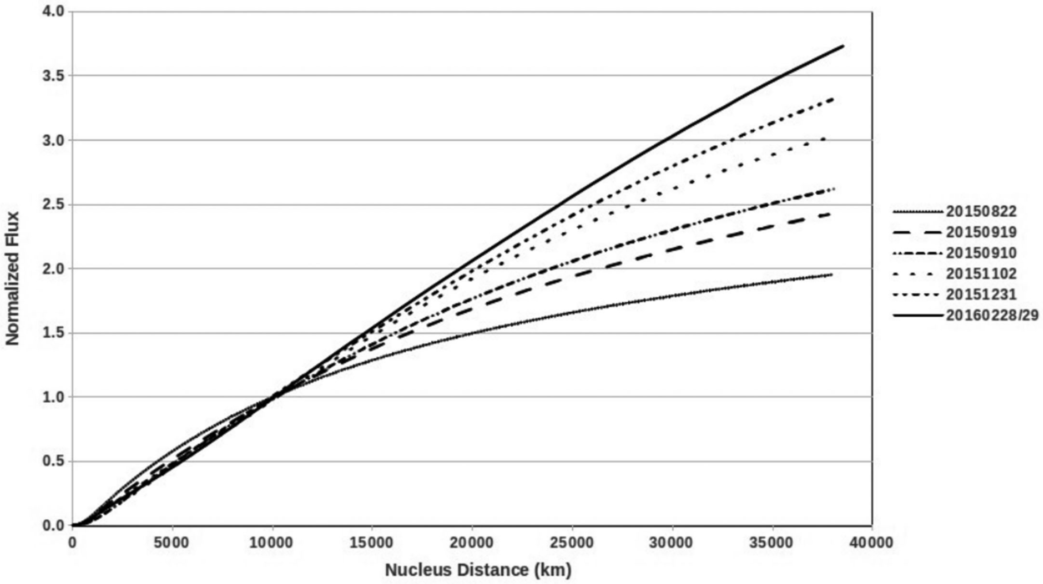

Figure 6. Normalized averaged radial coma profiles of 67P – changes with time. The figure plots for various dates during our observing campaign radial flux profiles from the coma center to about 38 000 km project nucleus distance. The individual graphs show the average coma flux in the measurement aperture of increasing nucleus distance. For comparison the flux values are normalized to unity for aperture size 10 000 km.

shown as of 2015 late September to December. It is noted that also the fan structures seen in the dust coma of the comet do not indicate significant changes, thus supporting a more continuous dust activity of 67P. Consequently, a linear ($\beta = 0.04$) or HG-type ($G = 0.15$) phase darkening describe best the post-perihelion brightness evolution of the comet for the time interval 2015 late September to 2016 early May. The maximum afρ of about 1300 cm shortly after perihelion corresponds to about the same amount of dust production in kg s^{-1}, if one assumes the empirical calibration of A'Hearn et al. (1995) that for 67P is not yet verified. This estimation strongly depends on the adopted phase darkening of the comet and of course on various other properties of the coma dust and may, at best, provide only an order of magnitude reference.

Radial coma flux profiles*:* the overall status of the dust coma is assessed by measuring the radial flux profile of the comet in concentric circular apertures, centred on the brightness peak in the coma. WWFI *r*-filter images of 67P are chosen for this analysis, since they are usually exposed longest and show best the dust distribution in the coma. Moreover, they are less or only very weakly contaminated by coma gas and are by far the most abundant compared to WWFI *i* images in our data set. Fig. 6 shows examples of the radial coma profiles measured throughout the observing campaign. It is noted that for all observing epochs, the profile slope becomes flatter with increasing distance from the nucleus. Due to radiation pressure, more sensitive, lighter and smaller grains are pushed stronger into antisolar direction such that they are missing in the size distribution at larger distances from the nucleus, in particular in the direction to the Sun. Hence, the radial profile gets flatter for larger distance. For a quantitative assessment of the profile, the exponent of the radial flux decrease is fitted to the measured radial profile for different distance ranges in the coma, i.e. log flux versus log aperture

Downloaded from https://academic.oup.com/mnras/article-abstract/462/Suppl_1/S376/2447817
by MPI Solar System Research user
on 03 September 2018

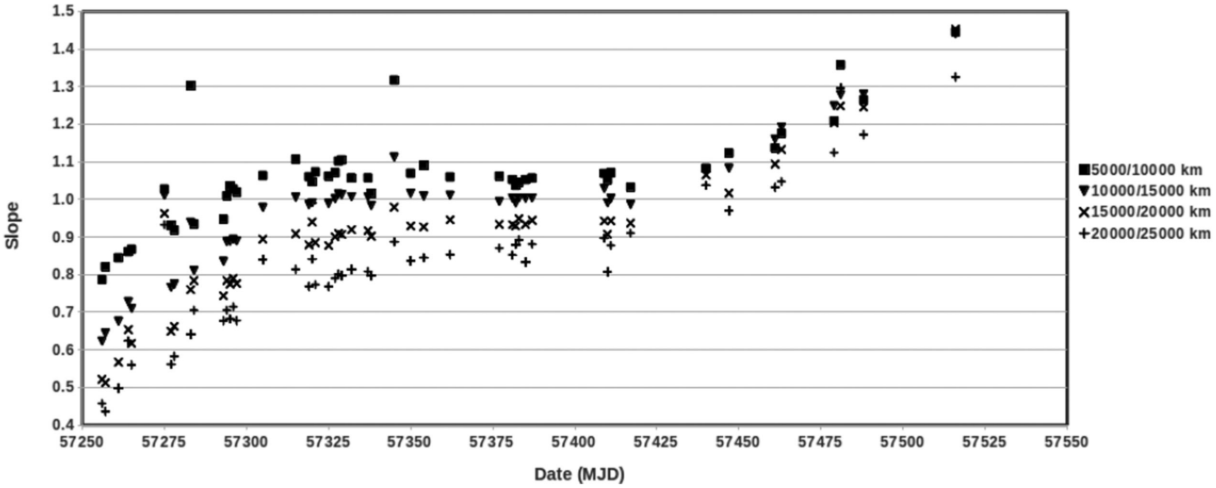

Figure 7. Radial slopes of the average coma profile of 67P versus time. The slope parameter is fitted to the profile in *r*-filter images over different distance ranges in the coma, i.e. between 5000 to 10 000 km, 10 000 to 15 000, 15 000 to 20 000 km and 20 000 to 25 000 km. Outlier values (on 2015 September 19, 2015 November 19, 2016 April 3) are due to bad seeing (3 arcsec and more) conditions.

radius for 5000–10 000, 10 000–15 000, 15 000–20 000 and 20 000–25 000 km projected distance in the cometary coma. The results are tabulated in Table 3 and plotted in Fig. 7.

From 2015 end of September to at least the end of December, the dust coma of 67P appeared to be globally in ‘quasi-steady-state’, since the radial exponents of the flux profiles were close to unity. As of 2016 late January and more pronounced during the subsequent months, the radial exponent of the measured inner most coma region (5000–10 000 km) – as well as the outer ones - increased above 1. The dust trail in the aperture radius, although at higher relative level with respect to the coma light than closer to perihelion, has a shallower brightness gradient than measured in the overage coma profile and is thus not responsible for the steeper gradients in the average coma profiles. This indicates that the ‘quasi-steady-state’ period for the coma dust had ended. With increasing solar distance, the dust leaving the gas–dust coupling zone around the nucleus has slower initial expansion velocity into the coma. Then, its travelling time for a passage through the innermost measurement aperture amounts to several days to a few weeks, meaning that the dust is piling up in the inner part of the coma, while the outer part contains the dust released earlier and with higher expansion speed. As a consequence, the radial slope in the coma profile increases above unity. A similar phenomenon, i.e. a very steep radial coma profile, was seen in 67P at solar distances around 3 au, when the comet approached the Sun in 2008 (Tozzi et al. 2011). The authors explained the observations by a very steep drop of the dust expansion velocity with exponents for the solar distance dependence between 4.2 and 4.9.

From 2015 August 21 to about mid-September, the exponent of the averaged radial dust coma profile is well below 1 for all distance ranges measured, reaching values of 0.8–0.45 at the beginning of the campaign. Ignoring albedo changes of the dust, this result implies that dust leaving the outer limit of the measurement aperture in the coma has a higher light scattering cross-section than the one entering the inner edge. Generating additional light scattering cross-section of the coma dust is possible if dust grains disintegrated throughout the coma of 67P. Hence, our measurements of the radial profiles in the coma of 67P suggest that dust fragmentation occurred within about one month after the perihelion passage of the comet. Dust fragmentation by electrostatic forces (Boehnhardt & Fechtig 1987; Boehnhardt 1989) is unlikely since the charging conditions do not vary a lot with solar distance such that it should continue to affect the radial profile even at larger distances. Indeed, Fulle et al. (2015) argue for electrostatic fragmentation of the dust when 67P was at larger distances from the Sun inbound. If this process still plays a role beyond the first month post-perihelion, it would be masked by the general evolution of the dust in the coma of 67P such that it is no longer discernible in the ground-based observation alone. Boehnhardt & Fechtig (1987) have proposed an alternative fragmentation scenario based upon the disintegration of larger grains into smaller building stones due to the evaporation of gluing material in larger aggregates. This process is likely temperature-driven and thus depending on the solar distance of the comet. Another process that may cause grain disruption is aggregate bursting due to acceleration of the grain rotation by solar irradiation on irregular-shaped dust grains (windmill effect; Paddack 1969; Paddack & Rhee 1975). Despite that a quantitative assessment of the efficiency of this effect for the dust in 67P is difficult, it should result in lower efficiency with increasing solar distance of the comet.

Cometary tail*:* over the whole observing period the tail of 67P appears as a narrow fuzzy extension in the north-western quadrant of the images, as of late October with a sharply peaked embedded axis of maximum brightness. It extends beyond the edge of the field of view of our exposures, several 100 000 km away from the nucleus (Fig. 8). The tail is more diffuse towards the southern edge and at the comet head, it connects to the coma isophotes.

In the Wendelstein images of 67P, narrow linear and kinked structures, indicative for ionic features of the plasma tail, are not identified. We thus believe that the tail appearance in the images is produced by dust -reflected sunlight. The position angles (PAs) of the main tail axis (PTA), represented by the line of maximum brightness is measured in the images close to the nucleus position and are tabulated in Table 6 together with the PAs of the extended radius vector of the comet (PSANG) and that of the negative direction of the comet’s heliocentric velocity vector (PSAMV), both projected on to the sky of the observer. PSANG is usually indicative for the tail region containing ‘young’ dust, released days to a few weeks before the observing epoch, as well as for the approximate direction of the ion tail. PSAMV is more representative for the location of older dust grains in the tail, released months in the past. Table 6 also provides

Downloaded from https://academic.oup.com/mnras/article-abstract/462/Suppl_1/S376/2447817
by MPI Solar System Research user
on 03 September 2018

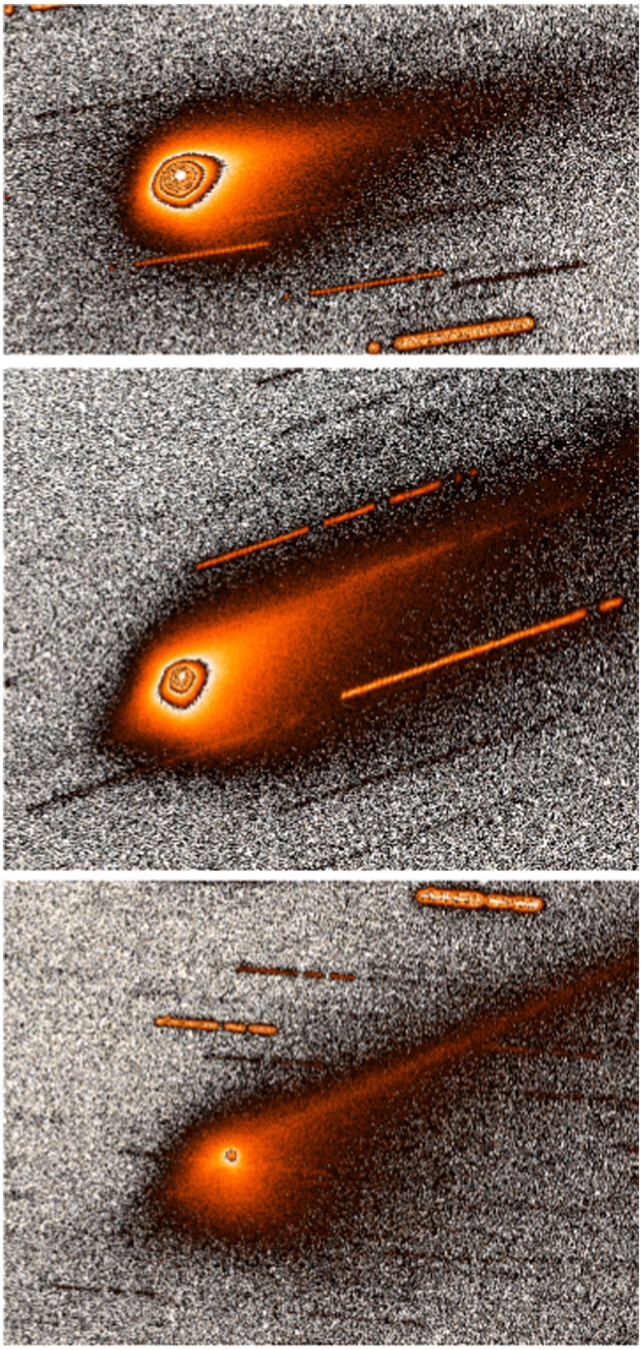

Figure 8. 67P dust tail appearance and geometry during three nights over the observing interval. The panels (in isophote-like representation) show the average composite images of the WWFI *r*-filter exposures of the respective nights. Stars and background objects appear as 'strings of pearls' in the images. Image orientation: north is up, east is to the left. Top panel: 2015 September 10, 20 min total integration time, field of view 284 000 × 156 000 km; Middle panel: 2015 November 11, 52 min total integration time, field of view 286 000 × 228 000 km; Bottom panel: 2016 April 10 to 11, 74 min total integration time, 341 000 × 252 000 km field of view.

the information on PAs for the so called dust synchrones in the tail region. Synchrones are the locations of dust grains of different solar radiation pressure sensitivity, but released at the same time from the nucleus. The synchrone PAs of 67P were estimated from the Finson–Probstein calculations of its dust tail (Finson & Probstein 1968; Beißer & Boehnhardt 1987). The table lists the synchrone PAs for dust, released 10 d before observing epoch (labelled DT = 10), thus representing the young dust in the tail, for dust released at perihelion (labelled $T = 0$) representing the period close to highest activity of the nucleus, and for dust released 400 d before perihelion (labelled $T = -400$), representing old dust emitted from the nucleus when the comet was beyond 3 au from Sun inbound. Since the changes of PAs are relatively slow with time, Table 6 shows the results for a representative set of the available observing epochs, distributed over the whole observing interval of 67P from 2015 late August to 2016 early May.

The interpretation of the tail structure in the Wendelstein images is in good agreement with the time evolution of the measured PAs of the tail of 67P, as compared to PSANG and PSAMV (see Table 6). Since the orbit inclination of 67P is low (7°), the dust tail is mostly seen side-on with low out-of-plane viewing angles from Earth (below 5°). Only during the opposition time interval (2016 January–May), the tail region covers a wider range of PAs. From the comparison of the tail PAs measured (PTA) with the PSANG and PSAMV values as well as with the PAs of synchrones in Table 6, we conclude that both the young and the older dust tail overlap in the PA range spread by PSANG and PSAMV. From 2015 late August to about mid-October, the main axis of the dust tail close to the nucleus is defined by 'young' dust released within a few weeks before the observing epoch. At that time, the tail is more diffuse which is assumed to be due to the higher out-of-orbital-plane velocity of the grains released closer to perihelion. A minor curvature to smaller PAs further away from the nucleus indicates the presence of 'older' (and larger) dust grains in the tail region, frequently associated with the dust trail of the comet. Around the period of the comet orbital plane crossing by the Earth (2015 mid-October to end November; plane crossing happened on 2015 November 13), the young and the old dust fully overlap in the tail region. Thereafter, i.e. as of 2015 early December until the end of our observing period of the comet in early 2016 May, the tail axis is associated with the 'older' dust, released several 100 or even more days before perihelion passage (2015 August 13). It is noted that the sweeping of the 'young' dust tail from the northwestern to the southeastern quadrant around comet opposition is not obvious from the Wendelstein exposures. In particular, the 'young' dust tail is – at best – only marginally detectable in antisolar direction in 2016 April to early May, despite an amplification of its scattering cross-section due to another comet orbital plane passage by the Earth (2016 May 10). This may be due to the very much reduced activity of 67P beyond 2.5 au from the Sun (see Fig. 5 and Table 3) as compared to the months following perihelion passage.

Coma: the dust coma of 67P is best depicted in the WWFI *r*-filter images. The isophote pattern appears neither perfectly circular nor perfectly oval, which can be considered as an indicator for a rather uniform activity across the nucleus surface. Instead, it shows moderate 'bumps' indicative for localized coma features of enhanced dust reflectivity. The coma structure enhancement techniques applied to the images (i.e. radial renormalization and adaptive Laplace filtering, see Section 3) reveal a coma pattern with two (pattern X1) or three (pattern X2) fan-like dust structures embedded in the bumpy isophote appearance of the comet - see Fig. 9 for the appearance of pattern X1 and X2 and Table 7 for characteristic information of the fan structures in the patterns.

Pattern X1 has a fan (labelled B in Table 7 and Fig. 9) of about 15°–30° opening angle, pointing approximately in east-southeastern direction and another fan (labelled C in Table 7) of 10°–20° opening angle, pointing approximately to the south. Both fans B and C vary slowly with time in their near-nucleus PAs and in their approximate

Downloaded from https://academic.oup.com/mnras/article-abstract/462/Suppl_1/S376/2447817
by MPI Solar System Research user
on 03 September 2018

Table 6. PA of the dust tail region of 67P, representing the observing interval of the comet from 2015 late August to 2016 early May. The table columns list (from left to right): the observing date, the PA of the extended radius vector of the comet (PSANG), the PA of the negative direction of the comet's heliocentric velocity vector (PSAMV), the PA PTA of the main tail axis measured in the images, the angles PTA-PSANG and PTA-PSAMV, the PA of synchrones for dust released 10 d before observing epoch (PA DT = 10), at perihelion passage (PA T = 0) and 400 d before perihelion (PA T = −400) and the angular differences between PTA and the three synchrones, i.e. PTA-DT = 10, PTA-T = 0 and PTA-T = −400. PTA is measured to +/−2°, the other angles are accurate to +/−1°.

Date (UT)	PSANG (°)	PSAMV (°)	Tail Axis PTA (°)	PTA-PSANG (°)	PTA-PSAMV (°)	PA DT = 10 (°)	PA T = 0 (°)	PA T = −400 (°)	PTA-DT = 10 (°)	PTA-T = 0 (°)	PTA-T = −400 (°)
2015/08/22	278	269	281	3	12	276	277	270	5	4	11
2015/08/23	279	269	283	4	14	277	277	270	6	6	13
2015/08/27	281	272	284	3	12	279	278	272	5	6	12
2015/08/30	282	273	283	1	10	280	279	273	3	4	10
2015/08/31	282	273	283	1	10	280	279	273	3	4	10
2015/09/10	286	277	290	4	13	284	283	277	6	7	13
2015/09/12	287	278	290	3	12	285	284	278	5	6	12
2015/09/19	289	281	294	5	13	286	285	281	8	9	13
2015/09/30	292	285	295	3	10	290	288	285	5	7	10
2015/10/10	294	288	293	−1	5	293	290	287	0	3	6
2015/10/20	295	290	297	2	7	294	292	290	3	5	7
2015/11/01	296	293	300	4	7	295	294	293	5	6	7
2015/11/12	296	296	303	7	7	296	295	295	7	8	8
2015/11/24	296	298	304	8	6	295	296	297	9	8	7
2015/12/06	295	300	305	10	5	295	297	298	10	8	7
2012/12/21	294	303	305	11	2	294	297	300	11	8	5
2012/12/29	293	304	302	9	−2	293	297	300	9	5	2
2015/12/31	292	304	303	11	−1	293	297	300	10	6	3
2016/01/22	288	305	304	16	−1	289	297	301	15	7	3
2016/01/30	286	305	305	19	0	287	297	300	18	8	5
2016/02/22	273	303	300	27	−3	277	295	300	23	5	0
2016/02/28/29	261	301	300	39	−1	270	295	299	30	5	1
2016/03/16	170	300	300	130	0	233	294	299	67	6	1
2016/04/01	131	298	296	165	−2	136	294	295	160	2	1
2016/04/10/11	124	297	295	171	−2	126	294	295	169	1	0
2016/05/07/08	116	296	297	181	1	116	295	295	181	2	2

brightness ratio relative to the mean coma brightness, estimated at about 5000 km distance from the nucleus. The enhanced images (for examples, see Fig. 9) allow the measurement of the near-nucleus PAs of the fan-like coma structures and they also show their further extension in the coma out to several 10 000 km projected nucleus distance. Straight and positively curving (increasing PA counted east over north) fans are noticed.

Pattern X2 contains the two fan-like structures B and C of pattern X1 and in addition, a short, about 10°–20°-wide fan A, pointing in approximately east-northeastern direction (see Table 7 and Fig. 9). Pattern X1 was observed from 2015 August 22 (earliest observing date at Mt. Wendelstein for 67P) until late October. Pattern X2 followed after X1 and lasted at least until 2016 mid-April.

In the following, we describe the individual fan-like dust structures in the coma and assess the possible origin for the dust emission. For the latter, we apply dust coma modelling after Beisser & Drechsel (1992) that is based on a Monte-Carlo Finson–Probstein algorithm for dust, emitted from different locations on a rotating spherical nucleus. Since the nucleus of 67P has a bi-lobate shape (Sierks et al. 2015), our modelling results cannot adequately represent the dust emission geometry on the nuclear surface, but they are taken as an approximation for the dust flow geometry at larger distances (>1000 km, the typical size of the seeing disc in ground-based observations) from the nucleus beyond the dust–gas coupling and acceleration zone. For the rotation motion of the nucleus, the axis orientation and rotation period given by Sierks et al. (2015) are applied. Since – by the time of writing - the Rosetta images of the 67P dust and gas activity close to the nucleus for the time period 2015 August–2016 May are not yet publicly available, a correlation assessment of structures seen in ground-based and Rosetta images was not performed and remains to be done in the future. It is noted that the appearance of the individual fan-like structures described below did not change noticeably during the observing intervals of the individual observing nights. This indicates that the nucleus rotation did not modulate the fan-like coma structures on time-scales of hours, i.e. during a single nucleus rotation.

Fan A: fan A evolves only as of 2015 early November. It occurred first at about 60° PA as a narrow, straight and several 1000 km long feature. With time, it became more extended and it converged towards eastern direction, keeping always a straight appearance. It reached maximum intensity ratios of up to 1.15 compared to the average coma profile at 5000 km distance. The fan modelling suggests a near-equatorial location for the dust-emitting region of fan A.

Fan B: this fan structure resided in the southeastern quadrant of the coma during the whole observing period. The opening angle shrank after about orbital plane passage by the Earth around 2015 mid-November. The fan curvature was positive (counter-clockwise) until 2015 November, thereafter it got rather straight until the end of the observing interval. It is noted that during the first two months of the observing period, the tailward curvature of the dust in the fan was rather sharp at about 25 000 km in the sunward coma hemisphere,

Downloaded from https://academic.oup.com/mnras/article-abstract/462/Suppl_1/S376/2447817 by MPI Solar System Research user on 03 September 2018

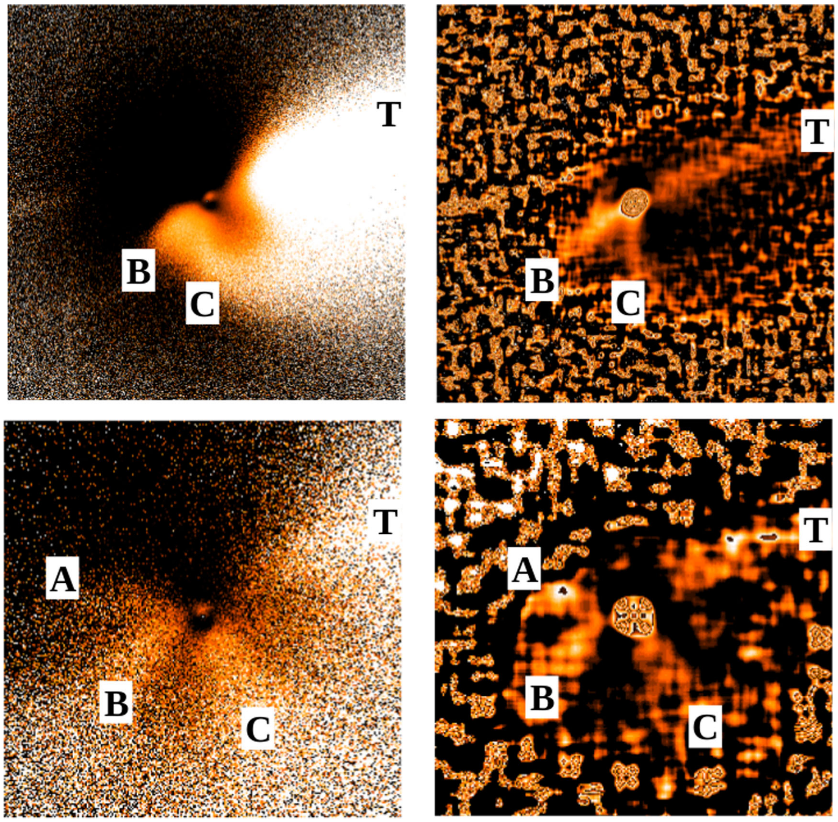

Figure 9. Patterns X1 and X2 of fan-like structures in the coma of 67P. The top row shows the radially renormalized ratio (left) image and the Laplace-filtered image (right) of 67P on 2015 September 30 as an example of the X1 pattern in the coma. Image scale is 130 000 × 130 000 km at the comet. The bottom image pair provides the respective example image for the X2 pattern in the coma as observed on 2016 March 16. Image scale is 58 000 × 58 000 km at the comet. For all images: north is up and east to the left. The coma fans are labelled by letters A, B, C. The dust tail is indicated by letter T.

suggesting the presence of dust grains of expansion velocity up to 50–100 m s^{-1} for a solar radiation pressure sensitivity of up to 0.5. Up to the time of orbital plane passage by the Earth (2015 November 13), a short northward extension of the fan evolved a few thousand kilometers projected distance from the coma center, indicating dust grains expanding into low-obliquity directions towards the north of the sub-solar latitude. The Monte-Carlo modelling suggests that fan B is related to dust emission from mid-southern latitudes (40°–50° south). The short northward extension of the fan could result from activity from low southern latitudes, possibly even from the source regions of fan A. This implies that the fan activity started at relatively high solar illumination angles of the source region.

Fan C*:* this fan-like structure is visible in southern direction over almost the whole observing period when 67P images were taken, i.e. from 2015 late August until 2016 early April. It is not identified in the 2016 May images; however, these exposures have only low signal-to-noise ratios such that it may have escaped detection. The opening angle is about 15°–20° and it reached highest brightness ratios around 2015 October to November. Fan structure C showed positive curvature. However, it displayed a straight figure in the near-nucleus region during the first 2.5 months of our observations of 67P (up to 2015 late October). It turned into tail direction at about 40 000 km projected nucleus distance. The fan modelling suggests that coma structure C is produced by the activity in high southern latitudes (most likely 60°–80° south) on the nucleus. The opening angle requires either a certain latitude and/or longitudinal extension or a significantly long daily activity cycle of the related surface region. The curvature of the fan C suggests expansion velocities in the range of 50–100 m s^{-1} for dust grains of a solar pressure sensitivity of up to 0.5.

Dust arc on 2015 August 23: comparison of Laplace-filtered images of 67P, obtained on 2015 August 22 and 23 shows a temporary structure in the northeastern coma quadrant (Fig. 10). The structure consists of a narrow (<1000 km wide), linear jet-like feature, extending at a PA of about 20° up to projected nuclear distances of about 13 000 km. At that location, an ∼2500 km wide arc-like structure connects to the jet, pointing at PA of about 45° and extending for another 11 000 km. Both jet and arc are detected on 2015 August 23, but they are not seen in 67P images taken on 2015 August 22 and 26, the two observing epochs in our dataset closest in time to 2015 August 23. The temporary pattern on 2015 August 23 also results in more extended isophotes in the respective PA range (Fig. 10, top panels) that could be understood as being due to an enhanced amount of dust in this part of the coma compared to the day before. However, since only WWFI *r*-filter images are taken on 2015 August 23, a gaseous origin of the temporary jet- and arc-like structures cannot be excluded, but appears to be unlikely given the rather confined geometry of both features. As can be seen in Fig. 1 and Table 1, a small brightness increase of about 0.1 mag is noted on 2015 August 23 compared to the coma brightness of the day before. However, since this amplitude is at the level of the estimated intrinsic average accuracy of our coma photometry and since a very similar brightness level of the comet is measured on 2015 August 26, we do not have a clear evidence for a relationship between the measured photometric brightness increase and the appearance of the arc and jet structure. The ratio image between 2015 August 23

Downloaded from https://academic.oup.com/mnras/article-abstract/462/Suppl_1/S376/2447817
by MPI Solar System Research user
on 03 September 2018

Table 7. Characteristics of the 67P dust coma fans. The table columns list (from left to right): the date of the observation (UT), the PA of the extended radius vector of the comet (PSANG in deg), the PA of the negative direction of the comet's heliocentric velocity vector (PSAMV), the subsolar latitude on the nucleus of 67P (south = negative; deg), the near-nucleus PA of a fan produced by an active region on the southern rotation pole of the nucleus (deg), the fan pattern label (X1 or X2 as described in the text), the near-nucleus PAs of fan structures A, B, C (measured north over east; deg), the near-nucleus opening angle of the fan-like structures A, B, C, the overall curvatures of the fan-like structures (s = straight, p = counter-clockwise, n = clockwise) and the intensity ratio of the fan maximum brightness at about 5000 km projected distance to the nucleus compared to the average coma brightness level at that distance for fan-like structures A, B, C. NM indicates non-measurable property of the fan-like structures, ? identifies a tentative, but uncertain estimation.

Date (UT)	PSANG (°)	PSAMV (°)	Subsolar latitude (deg)	Angle Rotation axis (°)	Pattern type	Pasition angle A (°)	Pasition angle B (°)	Pasition angle C (°)	Openening angle A (°)	Openening angle B (°)	Openening angle C (°)	Curvature A	Curvature B	Curvature C	Intensity ratio A At 5000 km	Intensity ratio B At 5000 km	Intensity ratio C At 5000 km
2015/08/22	278	269	−51	165	X1	NM	101	188	NM	30	15	NM	p	sp	NM	1.3	1.2
2015/08/23	279	269	−51	165	X1	NM	103	189	NM	30	15	NM	p	sp	NM	1.3	1.2
2015/08/27	281	272	−52	165	X1	NM	104	189	<10	30	15	NM	p	sp	NM	1.3	1.25
2015/08/30	282	273	−52	164	X1	NM	103	190	NM	30	15	NM	p	sp	NM	1.3	1.25
2015/08/31	282	273	−52	164	X1	NM	103	190	NM	30	15	NM	p	sp	NM	1.3	1.25
2015/09/10	286	277	−52	160	X1	NM	114	166	<10	30	15	NM	p	sp	NM	1.3	1.25
2015/09/12	287	278	−52	159	X1	NM	114	168	NM	30	15	NM	p	sp	NM	1.3	1.25
2015/09/19	289	281	−51	159	X1	NM	116	172	NM	30	15	NM	p	sp	NM	1.3	1.25
2015/09/30	292	285	−48	158	X1	NM	118	175	NM	30	20	NM	p	sp	NM	1.35	1.3
2015/10/10	294	288	−44	156	X1	NM	118	175	NM	25	20	NM	p	sp	NM	1.4	1.3
2015/10/20	295	290	−41	156	X1	NM	123	173	NM	25	20	NM	p	sp	NM	1.4	1.35
2015/11/01	296	293	−36	155	X2	60	128	175	20	20	20	s?	p	sp	NM	1.4	1.4
2015/11/12	296	296	−32	158	X2	63	125	180	20	20	20	s	p	sp	NM	1.35	1.4
2015/11/24	296	298	−28	158	X2	65	130	183	20	20	20	s	p	sp	NM	130	1.35
2015/12/06	295	300	−24	159	X2	70	128	190	20	15	20	s	sp	sp	NM	1.2	1.3
2012/12/21	294	303	−20	160	X2	74	126	189	15	15	15	s	sp	s	NM	1.15	1.15
2012/12/29	293	304	−17	161	X2	77	120	196	15	15	15	s	sp	s	1.05	1.25	1.15
2015/12/31	292	304	−17	161	X2	74	123	199	15	15	10	s	sp	s	1.1	1.15	1.1
2016/01/22	288	305	−11	161	X2	74	120	200	15	15	10	s	s	s	1.1	1.15	1.05
2016/01/30	286	305	−9	161	X2	77	121	202	15	15	10	s	s	s	1.1	1.15	1.05
2016/02/22	273	303	−5	160	X2?	NM	118	NM	NM	15	NM	NM	NM	NM	NM	1.1	NM
2016/02/28/29	261	301	−3	159	X2	77	117	220?	15	15	15	s	sp	s	1.15	1.15	1.05
2016/03/16	170	300	−1	157	X2	78	117	210	15	15	15	s	sp	s	1.15	1.2	1.1
2016/04/01	131	298	2	156	X2	80	115	205	10	20	20	s	s	sp	1.1	1.2	1.15
2016/04/10/11	124	297	3	156	X2	75	108	202	10	20	20	s	s	s	1.1	1.2	1.15
2016/05/07/08	116	296	7	156	X2	75	105	NM	NM	NM	NM	s	s	NM	NM	NM	NM

Downloaded from https://academic.oup.com/mnras/article-abstract/462/Suppl_1/S376/2447817
by MPI Solar System Research user
on 03 September 2018

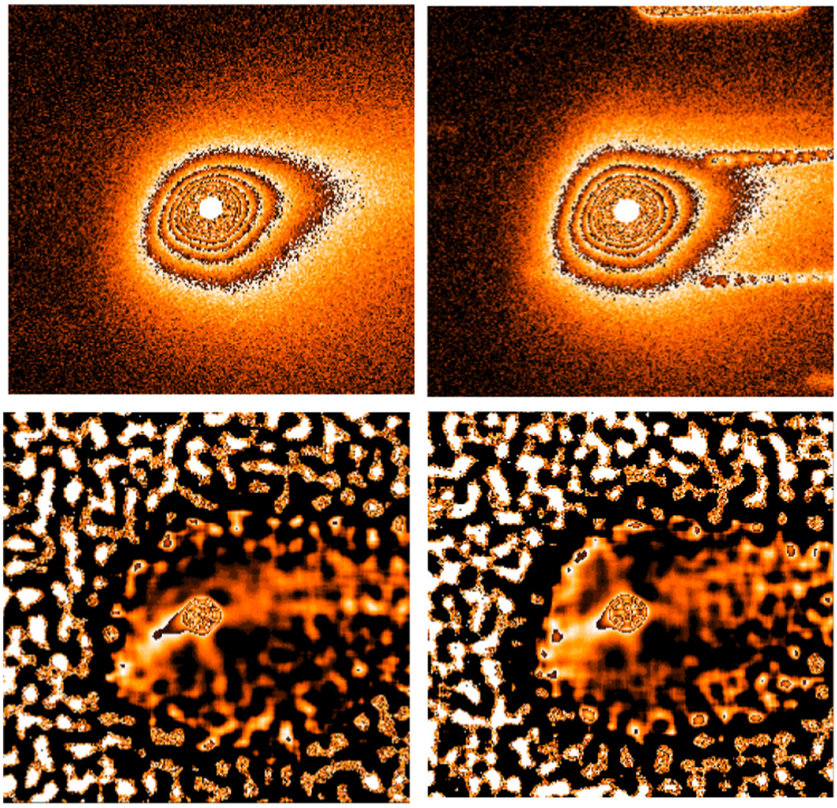

Figure 10. Dust arc in the coma of 67P. The images show the isophote pattern of the comet on 2015 August 22 (top left panel), the isophote pattern of the coma on 2015 August 23 (top right panel), and the respective adaptive Laplace-filtered versions of the comet image on both observing epochs (bottom left panel for 2015 August 22, bottom right for 2015 August 23). The isophote pattern on 2015 August 22 and 23 differ in the northeastern coma quadrant. The Laplace-filtered image of 2015 August 23 displays a straight short jet-like structure at near-nucleus PA 20° and an arc-let structure at the end of the jet, extending into southwestern direction. Both features are not present in the coma the day before. Image orientation is north up, East to the left, image scale is 63 000 × 61 000 km at the distance of the comet.

and 22 shows a local brightness increase in the northeastern coma quadrant that reaches a level of 1.7 and 1.3 in the regions of the shell and jet structure, respectively.

The connecting geometry of arc and jet suggests a physical relationship for their origins. Dust activity modelling suggests that the arc material expands from low positive latitudes between about $+5°$ to $+10°$. The similar projected distance of the arc from the nucleus and its uniform width can be understood by dust production of the arc material peaking at about the same time over a short time interval and over a latitude range of about 5° on the nucleus. Assuming that the dust emission event may have started 24 h earlier on 2015 August 22 (when the jet and arc structure are not seen in our images), the arc material may have expanded with a velocity of about 150 m s^{-1} and a velocity spread of the order of 30 m s^{-1}. The event must have been very short in time (an ejection activity peak of the order of half-hour or less) in order to allow for the confined arc appearance 24 h later. The jet-like structure seen in the images of 2015 August 23 suggests that the activity at the northern edge of the ejection region continued for at least 24 h. Up to now, it was not possible to associate unusual instrument measurements on-board Rosetta with the origin of the arc and jet-like features, since the mission data are not yet publicly available (and the orbiter instruments have not fully taken note of the event seen in the Wendelstein data, despite that it was reported to the project within a few days after the event). However, for an arc-jet scenario as outlined above, detection by Rosetta *in situ* and remote sensing instruments requires the orbiter to fly – in a few 100 km distance - across the proper surface area at the right moment very close in time when the event happened or to image the respective region of dust ejection at the right moment (order of a few minutes).

5 CONCLUSIONS AND DISCUSSION

Comet 67P was observed from the Mt. Wendelstein observatory by broadband imaging from 2015 August 22 to 2016 May 9. The images through the WWFI *r* filter show the dust coma and tail of the comet between 9 and 270 d after perihelion passage on 2015 August 13. Indications for the gaseous coma are noted for two observing epochs (2015 September 10 and 12) from colour difference in the *g*–*r* and *g*–*i* versus the *r*–*i* wavelength range. The dust colour corresponds to a moderately red spectral slope of about 8.5 per cent/100 nm for the WWFI *r*- and *i*-filter wavelength range. The dust activity of 67P, represented by the afρ parameter obtained from the measured coma brightness in the *r* filter, reached its maximum during the first weeks of our observing campaign and it dropped steeply and continuously as of the second half of 2015 September until the end of our campaign. A plateau in the afρ curve versus solar distance from 2016 end of January to April is interpreted as being due to the opposition surge of the light scattering phase function. A linear (with slope 0.04) or asteroid-like HG-type phase function (with $G \sim 0.15$) describes a uniform activity decrease of the comet with heliocentric distance exponent of 4.1–4.2. However, from our observations, a longer lasting activity bump or even a drop in the

Downloaded from https://academic.oup.com/mnras/article-abstract/462/Suppl_1/S376/2447817
by MPI Solar System Research user
on 03 September 2018

activity around opposition cannot be fully excluded depending on the dust phase function assumed.

The averaged brightness coma profiles displayed close to unity radial gradients from 2015 end of September until late December indicating a 'quasi-steady-state' dust coma. Before that time period, the radial slope of the coma brightness was below unity, which is interpreted as being due to the production of additional light scattering cross-section with nuclear distance, possibly from the dust aggregate fragmentation throughout the coma. In 2016, the averaged radial brightness profile of the coma got steeper than unity, which might be a consequence of a 'non-steady-state' coma due to a very much reduced dust expansion speed and thus an accumulation of dust activity in the inner coma. In this context, it is noted that for a dust expansion speed of 50–100 m s^{-1}, which may be considered representative for the time close to perihelion, the travelling time of dust grains through a 10 000 km radius measurement aperture is about 1–2 d. For slow changes in the dust activity versus time as it is seen in 67P, the coma is considered to be in a 'quasi-steady-state'. For expansion speeds reduced by a factor of 10 – which may be typical for the comet at larger distances from the Sun – the dust travelling time through the 10 000 km measurement aperture is of the order of 10–20 d, a situation when the coma is no longer in 'quasi-steady-state'. This also implies that the afρ values are to be taken as a kind of average value over a longer period of dust activity when changes of dust production and other dust parameters might occur and might impact the afρ result.

The dust tail appearance changed from a normal tail geometry before opposition to an antitail one after opposition in 2016 early March. Close to perihelion, the tail of 67P reflects mostly the distribution of younger dust overlapping the distribution of older dust. Around the time of orbital plane passage by the Earth in 2015 November, the older dust with grains produced more than a year before perihelion passage dominated the tail appearance until the end of the observing campaign in 2016 May.

Two patterns of coma structures are observed in 67P, i.e. one up to 2016 end of October, showing two fan-like dust features in the southern and eastern coma quadrants and one as of thereafter showing - in addition to the two others - a fan structure in the east-northeastern part of the coma. The three fans are explained as being due to the dust activity in high latitude (southern fan), mid-latitude (eastward fan) and near-equatorial (east-northeastern structure) regions of the nucleus. The latitude ranges found for dust activity in the fan-shape coma are consistent with the results published by Vincent et al. (2013) from the ground-based imaging before the Rosetta encounter with the comet. Both our modelling and the one performed by Vincent et al. apply a spherical nucleus shape and are thus not necessarily representative for a final solution using the bi-lobate shape and actual surface geometry of the nucleus of 67P. The association of near-nucleus cometary activity from Rosetta with the large-scale picture of the coma as seen, for instance, in Earth-based observations still has to be evaluated. The fan-shape coma as observed from Earth has to be traced back to the near-nucleus dust emission pattern as observed by Rosetta. As such, our analysis results represent at least approximately the dust expansion beyond a few 1000 km nuclear distance in the coma.

The global picture of 67P after perihelion passage 2015 resembles, in many aspects, the appearance during earlier apparitions of the comet, i.e. the dust activity (afρ versus time) and the fan-shape coma (see, for instance, Snodgrass et al. 2013, 2016 and references therein). This suggests that the activity pattern of 67P may not have changed much over the time period of a revolution around the Sun. This may apply as well for the rotation motion of the nucleus and the location of regions of enhanced dust emission from the nucleus.

An isolated dust ejection happened on the nucleus on 2015 August 22 and 23 resulting in an arc- and jet-like feature in the northwestern coma quadrant. The event may have been of very short duration, expanding the dust at high speed (order 100 m s^{-1}) from a region at low, but extended positive latitudes (5°–10°). An association of near-nucleus localized dust activity as measured by Rosetta and that seen in ground-based images was not yet attempted.

ACKNOWLEDGEMENTS

The authors of this paper want to thank Dr J. Koppenhoefer for his support in the provision of the Pan-STARRS1 catalogue data and Dr K. Beisser for making available the Monte-Carlo simulation software for the dust coma and tail of comets. We also wish to acknowledge the important contributions for this work resulting from the Pan-STARRS1 Survey catalogue data. The Pan-STARRS1 Surveys (PS1) have been made possible through contributions of the Institute for Astronomy, the University of Hawaii, the Pan-STARRS Project Office, the Max-Planck Society and its participating institutes, the Max Planck Institute for Astronomy, Heidelberg and the Max Planck Institute for Extraterrestrial Physics, Garching, The Johns Hopkins University, Durham University, the University of Edinburgh, Queen's University Belfast, the Harvard-Smithsonian Center for Astrophysics, the Las Cumbres Observatory Global Telescope Network Incorporated, the National Central University of Taiwan, the Space Telescope Science Institute, the National Aeronautics and Space Administration under Grant No. NNX08AR22G issued through the Planetary Science Division of the NASA Science Mission Directorate, the National Science Foundation under Grant No. AST-1238877, the University of Maryland, and Eotvos Lorand University (ELTE). This research was supported by the cluster of excellence 'Origin and structure of the universe' of the Deutsche Forschungsgemeinschaft DFG.

REFERENCES

Agarwal J., Müller M., Grün E., 2007, Space Sci. Rev., 128, 79
Agarwal J. M., Müller M., Reach W. T., Sykes M. V., Boehnhardt H., Grün E., 2010, Icarus, 207, 992
A'Hearn M. F., Millis R. L., Thompson D. T., 1984, Icarus, 55, 250
A'Hearn M. F., Hoban S., Birch P. V. Bowers C., Martin R., Klinglesmith D. A., III, 1986, Nature, 324, 649
A'Hearn M. F., Millis T. L., Schleicher D. G., Osip D. J., Birch P. V., 1995, Icarus, 118, 223
Beisser K., Boehnhardt H., 1987, Ap&SS, 139, 5
Beisser K., Drechsel H., 1992, Ap&SS, 191, 1
Boehnhardt H., Fechtig H., 1987, A&A, 187, 824
Boehnhardt H., 1989, Earth, Moon, and Planets, 46, 221
Boehnhardt H., Birkle K., 1994, A&A Suppl., 107, 101
Bowell E. et al., 1989, in Binzel R. P., Gehrels T., Matthews M. S. eds., Asteroids II. Univ. Arizona Press, Tucson, AZ, p. 524
Cremonese G. et al. 2015, A&A, 588, A59
Doressoundiram A., Boehnhardt H., Tegler S. C., Trujillo C., 2007, in Barucci M. A., Boehnhardt H., Cruikshank D. P., Morbidelli A., eds., The Solar System Beyond Neptune. Univ. Arizona Press, Tucson, AZ, p. 91
Ferrin I., 2005, Icarus, 178, 493
Finson M. J., Probstein R. F., 1968, ApJ, 154, 327
Fornasier S. et al., 2015, A&A, 583, A30
Fukugita M., Ichikawa T., Gunn J. E., Doi M., Shimasaku K., Schneider D. P., 1996, AJ, 111, 1748
Fulle M. et al., 2015, ApJ, 802, L12

Downloaded from https://academic.oup.com/mnras/article-abstract/462/Suppl_1/S376/2447817
by MPI Solar System Research user
on 03 September 2018

Gössl C., Riffeser A., 2002, A&A, 381, 1095

Gössl C., Bender R., Fabricius M., Hopp, Karasz A., Kosyra R., Lang-Bardl F., 2012, in McLean I. S., Ramsay S. K., Takami H., eds, Proc. SPIE Conf. Ser. Vol. 8446, Ground-based and Airborne Instrumentation for Astronomy IV. SPIE, Bellingham, p. A84463P

Hadamcik E., Sen A. K., Levasseur-Regourd A. C., Gupta R., Lasue J., 2010, A&A, 517, A86

Hopp U., Bender R., Grupp F. et al., 2014, SPIE Proceedings, 9145, A91452D

Ishiguro M., 2008, Icarus, 193, 96

Kelley M. S. et al., 2006, ApJ, 651, 1256

Kelley M. S., Reach W. T., Lien D. J., 2008, Icarus, 193, 572

Kelley M. S., Wooden D. H., Tubiana C., Boehnhardt H., Woodward C. E., Harker D. E., 2009, AJ, 137, 4633

Kidger M. R., 2004, A&A, 420, 389

Kosyra R., Gössl C., Hopp U., Lang-Bardl F., Riffeser A., Bender R., Seitz S., 2014, Exp. Astron., 38, 213

Lamy O. L., Toth I., Fernandez Y. R., Weaver H. A., 2004, in Festou M. C., Keller H. U., Weaver H. A., eds. Comets II. Univ. Arizona Press, Arizona, AZ, p. 223

Lamy P. L., Toth I., Weaver J. A., Jorda L., Kaasalainen M., Gutiérrez P. J., 2006, A&A, 458, 669

Lamy P. L., Toth I., Groussin O., Jorda L., Kelley M. S., Stansberry J. A., 2008, A&A, 489, 777

Lara L. M., de Leon J., Licandro J., Gutierrez P. J., 2005, Earth, Moon, and Planets, 97, 165

Lara L. M., Lin Z.-Y., Rodrigo R., 2011, A&A, 525, A36

Lowry S., Fitzsimmons A., Jorda L. et al. 2006, Bull. Am. Astron. Soc., 38, 492

Lowry S., Duddy S. R., Rozitis B., Green S. F., Fitzsimmons A., Snodgrass C., Hsieh H. H., Hainaut O., 2012, A&A, 548, A12

Magnier E. A. et al., 2013, ApJS, 204, 20

Müller M., 1999, PhD Thesis, Univ. Heidelberg

Paddack S. J., 1969, J. Geophys. Rev., 74, 4379

Paddack S. J., Rhee J. W., 1975, Geophys. Res. Lett., 2, 365

Schleicher D. G., Millis R. L., Birch P. V., 1998, Icarus, 132, 397

Schleicher D. G., 2006, Icarus, 181, 442

Schulz R., Stüwe J. A., Boehnhardt H., 2004, A&A, 422, L19

Sierks H. et al., 2015, Science, 347, aaa1044

Snodgrass C., Tubiana C., Bramich D. M., Meech K., Boehnhardt H., Barrera L., 2013, A&A, 557, A33

Snodgrass C. et al., 2016, A&A, 558, A80

Tedesco E. F. 1989, in Binzel R. P., Gehrels T., Matthews M. S., eds., Asteroids II. Univ. Arizona Press, Arizona, AZ, p. 1090

Tonry J. L. et al. 2012, ApJ, 750, 99

Tozzi G. P., Patriarchi P., Boehnhardt H., Vincent J.-B., Licandro J., Kolokolova L., Schulz R., Stüwe J., 2011, A&A, 531, A54

Tubiana C., Barrera L., Drahus M., Boehnhardt H., 2008, A&A, 490, 377

Tubiana C., Boehnhardt H., Agarwal J., Drahus M., Barrera L., Ortiz J. L., 2011, A&A, 527, A113

Vincent J. B., Lara L. M., Tozzi G. P., Lin Z.-Y., Sierks H., 2013, A&A, 549, A121

Weiler M., Rauer H., Helbert J., 2004, A&A, 414, 749

This paper has been typeset from a TEX/LATEX file prepared by the author.

Downloaded from https://academic.oup.com/mnras/article-abstract/462/Suppl_1/S376/2447817
by MPI Solar System Research user
on 03 September 2018